JOINING BEHAVIOUR OF CRYSTALLINE AND AMORPHOUS ZR-BASED ALLOY USING CU-BASED BRAZE

by

YEN-LIN CHIU

A thesis submitted to the
University of Birmingham
for the degree of
MASTER OF PHILOSOPHY

The School of Metallurgy and Materials
The College of Engineering and Physical Sciences
University of Birmingham
December 2012

ABSTRACT

The objective of this research was to understand the melting and wetting behaviour of braze alloys and mechanical properties of brazed joints for pure zirconium plates and the Zr-based bulk metallic glass (BMG), Vitreloy 105 ($Zr_{52.5}Cu_{17.9}Ni_{14.6}Al_{10}Ti_5$). Active brazing alloy, Cusil ABA ($Ag_{63}Cu_{35.23}Ti_{1.75}$), has been used to braze Zr plates in the Gleeble 3500 thermo-mechanical simulator under vacuum at 3 temperatures (840, 940 and 1000 ^oC) and with Vitreloy105 at 780 ^oC. The shear strength of the brazed Zr-plate increased at lower brazing temperatures; brazing of Vitreloy 105 plates was not successful as the brazing temperature, (Cusil ABA liquidus temperature) exceeded its crystallisation temperature T_x=440 ^oC leading to crystallization and embrittlement during to brazing. As a result, three BMG compositions ($Mg_{65}Cu_{15}Ag_{10}Tb_{10}$, $Zn_{40}Mg_{11}Ca_{31}Yb_{18}$ and $Ca_{65}Mg_{15}Zn_{20}$) as potential brazes for Vitreloy 105 with liquidus temperatures below the crystallisation temperature and high values of fracture strength have been selected to predict (using Thermo-Calc) the equilibrium reaction between substrate and braze prior to manufacture in order to estimate likely wettability and joint strength.

ACKNOWLEDGEMENTS

I would like to express my deep gratitude to my supervisor, Dr. Martin Strangwood, for his patient guidance and constructive suggestions. He shows his willingness to give his time on planning and developing this research work and leading me into the field of golf materials.

A very thankful for who supporting me during my research namely, Jas, Jeff, Andy, Paul and all the technical staff in the school of metallurgy and materials. They have been very enthusiastic about the training and supporting the experiment work. To our researching team Carl, Frank, Xi, Den, Mark and others that you have been very kind and give me a lot of support when I need it.

I like to give my special thanks to Mr. Jiang, who organized all the equipment for this work to continue my experiment, Professor Hsieh and his research team in MOES, National Sun Yat-Sen University in Taiwan.

Finally, I wish to thank my parents for their biggest support and encouragement throughout my study aboard and a very hard time within this year, last but not least, my lovely girlfriend, Shanti.

CONTENT

FIGURE

TABLE

EQUATION

SYMBOLS

$Q\ (\Delta G^a)$	Activation Energy
$k(t)$	Crystallised Volume Fraction
A	Frequency Factor
E	Linear Elastic Modulus
R	Universal Gas Constant
R_c	Critical Cooling Rate
t	Time
t_n	Nose Time of C-Curve in TTT Diagram
T	Temperature
T_g	Glass Transition Temperature
T_l	Liquidus Temperature
T_n	Nose Temperature of C-Curve in TTT Diagram
T_x	Crystallisation Temperature
T_{rg}	Reduced Glass Transition Temperature
ΔT_{xg}	Supercooled Liquid Region
D_{max}	Maximum Attainable Size of BMGs
J	Flux of Atoms
∇C	Laplacian of Concentration
D	Diffusion Coefficient
γ_{lv}	Liquid-Vapor Surface Tension
γ_{sl}	Solid-Liquid Surface Tension
γ_{sv}	Solid-Vapor Surface Tension
θ	Contact Angle Between The Solid and The Liquid
V	Velocity
M_h	Head Mass
m_b	Ball Mass
σ_y	Yield Strength
σ_f	Fracture Strength
ν	Poisson's Ratio

CHAPTER 1 INTRODUCTION

Joining Zr-based bulk metallic glasses (BMGs) for applications such as golf drivers has become an important research issue recently [1]. The joining of BMGs to themselves or other metallic systems, such as Ti-based alloys, requires a filler metal with adequate joint strength [2] and lower melting point and short processing time to avoid phase transformation from amorphous to crystalline and oxidation of Zr-based BMGs and Ti-based alloys. For this reason, experimenting into and prediction of reactions of Zr-based BMGs with potential filler metal by using crystalline zirconium brazed with the selected brazing alloy is needed to understand the fundamental reaction behaviour. Relating this behaviour to overall thermodynamic and kinetic models will allow appropriate selection of brazing alloys without excessive empirical testing.

Materials for golf driver have been developed from wood (used in solid heads) to metallic alloys (used in hollow heads) for increased driving distances and better accuracy [3]. Currently, titanium-based alloys are used as the main materials in golf driver heads. Zr-based BMGs have been used commercially, but only for the driver face, which failed to take advantage of their properties [3]. The aim of this study was to investigate the brazing behaviour of Zr-based BMGs in order to identify whether the BMG could be used more effectively in the crown of a golf driver head. Recently studies show that Cusil ABA, an active brazing alloy, can be used to braze Ti-based alloys [4] or ceramics, especially zirconia [5-6] to themselves or to other alloys. One intention of this study is to assess the feasibility of using Cusil ABA as a filler metal to braze zirconium and Zr-based BMGs (Vitreloy 105 in this study) to themselves.

1.1 Golf Drivers

Golf drivers (woods) are designed to send the golf ball the maximum distance off the tee consistently. The solid wood head limits the size (volume) of the driver head and requires excellent accuracy to aim the (small) sweet spot while striking the ball. In order to increase the size of the sweet spot and retain mass in the preferred 185 – 205 g range [7] the design of and materials used in the head have changed.

The history of golf driver heads has developed from original woods (persimmon or laminated maple) [3] with low yield stresses to aluminum-based alloys and stainless steel (17-4 PH) in the 1940s and 1950s respectively. Metallic driver heads have to be manufactured as hollow bodies so that the same head mass could be accommodated in a larger volume. A larger head volume gives a larger sweet spot, which should be easier to use by average players. From the mid-1990s, titanium-based alloys were used for larger hollow driver heads. The improvement of new materials and design goes beyond the sweet spot size effect as professional players, who strike the ball more accurately have also achieved greater distance. Figure 1 shows the average driving distances for players on the US PGA tour (two holes for ~ 190 golfers for all events in each year; 32,000 data points per year) from 1980 to 2008. The steeper increase from 1993 has been associated with the increased use of titanium-based alloys in hollow, oversized golf drivers. More recently, Zr-based amorphous alloys have been studied for use in golf driver heads [8,9].

The components of a hollow metallic golf driver head are the face, crown and sole. Each component of the head is manufactured by, most commonly, casting or forging techniques and joined by Electron Beam (EB) or Tungsten-Inert-Gas (TIG) welding methods for metallic components. Generally, driver heads are constructed from two (cast principally) or three pieces (cast or forged). The two-piece driver heads are cast as a face and sole in one

piece or face and crown in one piece to be joined to the crown or sole respectively. In three-piece heads, the face, crown and sole are shaped individually and joined to form the 3-dimensional shape.

1.2 Performance of Golf Driver Head

The introduction of Ti-based alloy drivers has led the USGA (United States Golf Association) and R&A (The Royal and Ancient Golf Club of St Andrews) to become concerned about potential larger increases in driving distance that may occur by using different materials and designs for the heads. This increase in drive distances would reduce the challenge of many courses and courses have responded by increasing the length of holes, e.g. Augusta National Golf Club for the Masters. The USGA introduced a limitation for drivers based on club head size (≤ 460 cubic centimetres) and CoR (coefficient of restitution < 0.83), which is based on the velocity ratio in 1998 [10]. The CoR is defined in Equation 1-1.

Equation 1-1

$$\mathrm{CoR} = \frac{\frac{V_{out}(M_h + m_b)}{V_{in}} + m_b}{M_h}$$

where M_h = head mass; m_b = ball mass. This measure is based on the ratio between horizontal inbound (V_{in}) and outbound velocity (V_{out}) components of a specific ball type, Pinnacle Gold, before and after impact with a free-standing driver head. Testing a driver head involves removing the shaft from the driver and substitutes an equivalent mass to the hozel before inverting the head and mounting it with face vertical. Testing involves firing the specific ball at the face at V_{in} of 48.768 ms^{-1} with 2 rpm of spin for improved accuracy. A single inbound speed is used as the CoR value is related to viscoelastic energy losses in the ball and so is strain rate dependent.

1.3 Increased Coefficient of Restitution (CoR)

A golf driver's CoR and performance are determined by the dimensions (thickness and area) of its components and the properties (elastic modulus and yield stress) of the materials from which they are constructed. One aspect of driver head design is to increase ball speed off the face for centred hits to maximise distance. In terms of kinetic energy (KE), to maximise ball release speed off the face, energy losses need to be minimised during transfer of KE from driver head to ball. The viscoelastic deformation of the golf ball (rubber-cored) is necessary to transfer KE via ball strain energy, but also introduces hysteresis resulting in energy losses that increase with increased strain in the ball. The effect of reduced rigidity of a driver head would be to give increased (linear elastic) club head deformation and reduced ball deformation during impact resulting in smaller energy losses and greater ball speed and distance. Stiffness of a driver head has been shown to be dominated by the crown [3] and so this component requires a material with sufficient strength (yield stress) to resist plastic deformation or fracture on impact whilst minimising thickness. Considering the geometry trends above, the use of materials with lower linear elastic modulus values would result in greater head deformation as well as reduced ball deformation.

1.4 Relationship of CoR to Frequency and Material Properties

Head stiffness has also been characterised using the resonant frequencies determined by sweet spot impact from a Brüel and Kjær (B&K) 4801 mini-shaker and a number of accelerometers around the face, crown and sole [3]. By using a constant shaker-head separation and a 1 ms top-hat voltage pulse, a 0.25 ms half sine-wave force was applied simulating ball impact strain rates, but not strains. Comparison of the frequency of the most intense vibration with CoR values (same club head sample used for both vibration and CoR

testing) allowed the relationship between frequency and CoR shown in Figure 2 to be determined.

The stiffness of the body would be reflected in the frequency of vibration. A low stiffness corresponds to a low frequency of vibration and results in a high CoR club. In addition, reducing the thickness and increasing the area of every section, but particularly the crown, will reduce the frequency according to general vibration dynamics. Change in mass could be neglected because the lower mass does not increase swing speed markedly. As noted above, thinning of a component requires a greater yield stress, whilst reduced modulus values would increase the elastic deformation of the club head. Thus, a material's performance index for use in the crown of high CoR drivers can be defined, Equation 1-2.

Equation 1-2

$$\text{Performance index} = \frac{\sigma_y}{E}$$

where σ_y is yield strength and E = linear elastic modulus. The relationship of the inverse frequency of the head and selected properties of the crown is described by Equation 1-3 [11]

Equation 1-3

$$\left(\frac{1}{\text{Frequency}}\right)_{\text{head}} \propto \left(\frac{\text{Area}}{\text{Thickness}^3}\right)_{\text{crown}} \left(\frac{\text{Hardness}}{\text{Elastic Modulus}}\right)_{\text{crown}}$$

For a driver head composed of face, crown and sole components joined to form a hollow 3-dimensional shape, equations 1-2 and 1-3 only apply if there is efficient transfer of deformation between components. This requires joints of similar stiffness to the components being joined, i.e. combined dimensions and modulus values should be similar to those of the face and crown. If joints with different thicknesses from the substrates are used and / or the modulus differs significantly then reflection of deformation waves occurs at the joint so that

head stiffness is dominated by the face not the crown. The resulting high head stiffness leads to lower than expected CoR values [2]. When amorphous Zr-based alloys have been used for the faces of golf drivers, they have been adhesively bonded in place requiring thick lugs that have prevented deformation being transferred to the crown and so low CoR values despite the high performance index value for Zr-based BMGs [6].

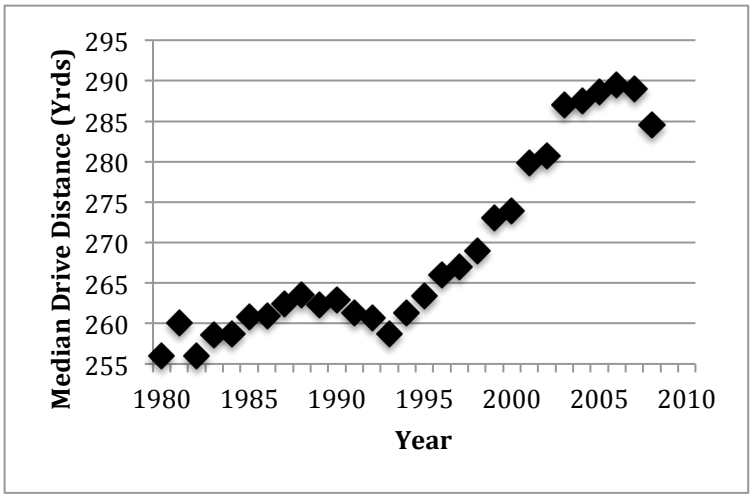

Figure 1 Average driving distance of professional golfer on the US PGA (Professional Golfers Association) tour from 1980 to 2008 [10].

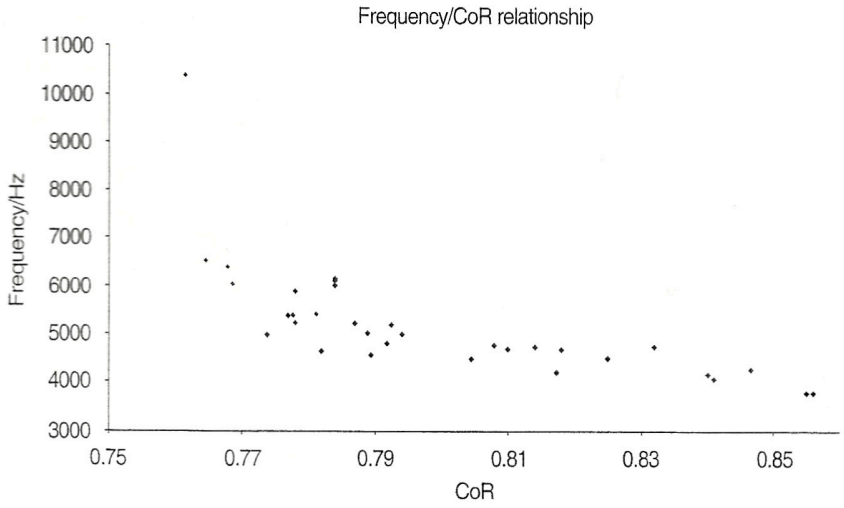

Figure 2 Relationship between frequency and CoR for hollow drivers [3].

CHAPTER 2 ZIRCONIUM-BASED BULK METALLIC GLASSES

Zr-based BMGs were the first type of metallic glasses to be prepared as large diameter rods in 1993 [12]. The excellent mechanical properties of Zr-based BMGs, which are high yield stress, low Young's (elastic) modulus and good glass formability in the supercooled liquid region, are the main attributes that make these BMGs attractive for structural applications [8].

Widmann [9] has pointed out that high performance driver heads are mainly designed from thin, large components using materials with high yield stress and low modulus of elasticity values, which give high performance indices (Equation 1-2). This would allow energy losses in the ball to be reduced and so increased drive distances for centred hits.

Steels and aluminium-based alloys are not used in current high performance driver design since they have low performance indices of 1.6 – 4.7, Table 1. Titanium-based alloys are currently used for high performance drivers. Beta Ti-based alloys have higher performance index values than others Ti-based alloys, such as $\alpha + \beta$ Ti-based alloy, of around 10.5.

Table 1 Properties of some materials used for golf driver heads [9].

Alloy	Elastic modulus (GPa)	Yield strength (MPa)	σ_y/E
316 Stainless steel	195	205-310	1.6
Al-Cu (Duralumin)	73	75-345	4.7
Ti-15V-3Al-3Sn-3Cr (beta)	85-120	800-1270	10.5
Ti-6Al-V (alpha+beta)	110-123	830-1100	8.8

The performance index of Vitreloy 105 in the as-cast condition is between 14.3 and 15.0 [9]. Elastic modulus values of Zr-based BMG alloys have been reported ranging from 40

to 112 GPa at room temperature [13-15]. In this study, the elastic modulus of Vitreloy 105 is from 99 to 105 GPa and the yield stress at room temperature of the fully amorphous phase has been determined to be around 1700 MPa. These characteristics are highly suitable for reduced ball energy loss on impact provided that the BMG is used in the crown and deformation can be transferred across the joint from the face. Vitreloy 105 offers a good GFA (Glass Form Ability), without involving toxic or precious metal elements and shows potential as a material for use in the design of golf drivers.

Golf applications involving impact require materials with high toughness. As-cast fully amorphous Zr-based metallic glasses offer toughness values comparable to aluminium- and titanium-based alloys. One of the most popular bulk BMGs developed, Vitreloy 1 ($Zr_{41.2}Cu_{12.5}Ni_{10}Ti_{13.8}Be_{22.5}$), has been reported to have fracture toughness values in the range of 55-131 MPa $m^{1/2}$ [16-18] in the amorphous state. Fracture toughness of fully amorphous Vitreloy 105 has been determined as 51 to 56 MPa $m^{1/2}$ [14], which is comparable to that of aluminium-based alloys and high strength steels. Once crystallised, the toughness is reduced to low values [19], so that, for use in golf drivers the BMG would have to be maintained in the amorphous state.

2.1 Glass-Forming Ability (GFA)

In bulk metallic glasses, the liquid metals are undercooled to a temperature below T_g, the glass transition temperature, when they form an amorphous phase. The nature of glass formation and GFA are key to developing new BMGs with improved properties and economic manufacturability in large quantities reproducibly [20].

Glass formation is possible only when liquid metal is cooled to below T_g faster than a critical cooling rate R_c that depends on the composition of the alloys and the section size for

the sample. As thickness increases then cooling rate becomes dominated by heat transfer within the solid so that a maximum attainable size, D_{max}, for glass formation can also be determined. The lower R_c or the larger D_{max} is, the better the GFA of that alloy system. One method to determine a critical cooling rate R_c would be from avoiding the nose of the solidification / crystallisation T-T-T (Time-Temperature-Transformation) diagram, Figure 3. Alternatively, criteria for glass formation for synthetic BMGs have been established from the alloy's physical properties and the amorphisation mechanism such as structural models, free electron theory, chemical factors (e.g. electron transfer, bond strength, and ionisation), phase diagram features, minimum volume criterion, atomic size criterion and solid solution model [8]. Several simple thermodynamic and structural GFA parameters have been deduced for various metallic systems from consideration of the kinetic processes, namely, the crystal growth rate, nucleation rate, or transformation kinetics. Inoue [8][21-23] has formulated three basic empirical rules for the formation of BMGs:

1. The alloy must contain at least three components. The formation of a glass becomes easier with an increasing number of components in the alloy system.

2. A significant atomic size difference should exist among the constituent elements in the alloys, where it is suggested that the atomic size differences should be greater than about 12 %.

3. There should be a negative heat of mixing among the constituent elements in the alloy system.

A few other simple parameters have been suggested to represent GFA, based on characteristic temperatures and other (physical) properties of the metallic glasses. The reduced glass transition temperature T_{rg} (T_g/T_l), the ratio of the glass transition temperature T_g to the liquidus temperature T_l, has been one [24]. The higher this value, the higher is the

viscosity and therefore the alloy melt could be easily solidified into a glassy state at a low critical cooling rate. This value will promote easy glass formation if an alloy composition with as high a value of T_g and as low a value of T_l as possible. However, if the actual solidification rate of the molten alloy is slower than the critical cooling rate for glass formation, the alloy will not form a glass even if its T_{rg} is very high.

A representative GFA indicator, the supercooled liquid region ΔT_{xg} (T_x-T_g), the temperature difference between the onset crystallisation temperature T_x and the glass transition temperature T_g), has been proposed for easy glass formers by Inoue et al. [25] based on the considerations of supercooled liquid stability against crystallisation. It has been reported [8] that the critical cooling rate for glass formation decreases with an increase in the ΔT_{xg} values. Table 2 presents a summary of ΔT_{xg}, T_{rg} and R_c values in various systems, such as Mg-, Zr-, and La-based BMGs. Table 3 summarises these characteristic temperatures for some typical conventional metallic glasses.

Glass formation is a balance between the stability of the liquid phase related to the short-range ordering of atoms in the molten state and the thermodynamic stability of the solid [26-28]. Another component is the resistance to crystallisation, which is determined by the driving force for crystallisation and the kinetics of nucleation and growth of crystalline phases.

Table 2 Summary of ΔT_{xg} ($T_x - T_g$), T_{rg} (T_g/T_l), critical cooling rate R_c and critical section thickness D_{max} for typical BMGs.

Alloy	ΔT_{xg}	T_{rg}	R_c (K/s)	D_{max} (mm)	Ref.
$Mg_{75}Ni_{15}Nd_{10}$	20.4	0.57	46.1	2.8	[29][30]
$Mg_{65}Ni_{20}Nd_{15}$	42.1	0.571	30	3.5	[29][30]
$Mg_{70}Ni_{15}Nd_{15}$	22.3	0.553	178	1.5	[29][30]
$Mg_{70}Cu_{25}Y_{10}$	54.0	0.551	50.0	7.0	[29][30]
$Zr_{65}Al_{7.5}Cu_{17.5}Ni_{10}$	79.1	0.566	1.5	4-16	[29][30]
$Zr_{41.2}Ti_{13.8}Cu_{12.5}Ni_{10}Be_{22.5}$	49	0.626	1.4	50	[31]
$Zr_{46.25}Ti_{8.25}Cu_{7.5}Ni_{10}Be_{27.5}$	105	0.525	28		[31]
$Zr_{52.5}Ti_5Cu_{17.9}Ni_{14.6}Al_{10}$	43.3	0.591	18.9-25	10	[31]
$Zr_{57}Ti_5Cu_{20}Ni_8Al_{10}$	51	0.608	10	10	[32]
$Cu_{60}Zr_{30}Ti_{10}$	50.0	0.619		4.0	[33]
$Cu_{54}Zr_{27}Ti_9Be_{10}$	42.0	0.637		5.0	[34]
$Ti_{34}Zr_{11}Cu_{47}Ni_8$	28.8	0.597	100	4.5	[29][30]
$Ti_{50}Ni_{24}Cu_{20}B_1Si_2Sn_3$	74.0	0.554			[35]
$La_{55}Al_{25}Ni_{20}$	64.3	0.521	67.5	3	[29][30]
$La_{55}Al_{25}Cu_{20}$	38.9	0.509	72.3	3	[29][30]
$La_{55}Al_{25}Ni_{10}Al_{10}$	79.8	0.56	79.8	5	[29][30]
$La_{55}Al_{25}Ni_5Cu_{10}Co_5$	76.6	0.566	18.8	9	[29][30]
$Ca_{65}Mg_{15}Zn_{20}$	24	0.561		6	[36]
$Ca_{65}Mg_{15}Cu_{20}$					[36]

Table 3 Summary of ΔT_{xg} ($T_x - T_g$), T_{rg} (T_g/T_l), critical cooling rate R_c for some typical non-BMGs.

Alloy	ΔT_{xg}	T_{rg}	R_c	Ref.
Ni	-	0.246	3.00×10^{10}	[37]
$Fe_{91}B_9$	-	0.369	2.60×10^{7}	[37]
$Zr_{65}Be_{35}$	11	0.503	1.00×10^{7}	[38]
$Ti_{63}Be_{37}$	-	0.496	6.30×10^{6}	[38]
$Mg_{77}Ni_{18}Nd_5$	7.8	0.484	4.90×10^{4}	[29][30]
$Mg_{90}Ni_5Nd_5$	22.8	0.464	5.30×10^{4}	[29][30]

2.2 TTT Diagram

The time-temperature-transformation (TTT) diagram (Figure 3) contains all the information needed to predict the formability and stability of any given glasses. It can be easily understood that, to form an amorphous solid material, the liquid should be cooled at a rate faster then critical cooling rate R_c, from the liquidus temperature through to a temperature below the glass transition temperature T_g. Critical cooling rates can be calculated in different alloy systems using equation 2-1 [8].

Equation 2-1

$$R_c \cong \frac{T_l - T_n}{t_n}$$

where, T_n and t_n are the temperature and time at the nose of the C-curve in the TTT diagram and T_l is the liquidus temperature.

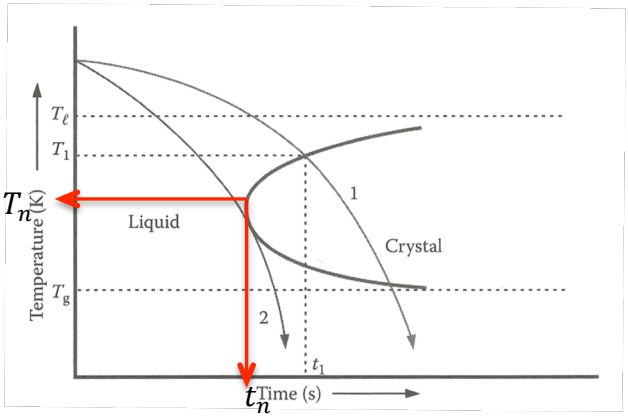

Figure 3 Schematic time-temperature-transformation (TTT) diagram for a hypothetical alloy system. Curve 1, represents a solidification rate producing a crystalline solid. The faster cooling rate, curve 2, is referred to as the critical cooling rate, R_c [8].

2.3 Eutectics

If an alloy system contains a eutectic, then this composition corresponds with the lowest molten temperature generally and much lower than the melting points of the individual components. The T_{rg} (T_g/T_l) value is a strong function of the composition and exhibits a generally high value at the eutectic composition compared with the rest of the system [8]. A number of studies on binary phase diagrams show that the eutectic composition will form the glassy state most easily in that alloy system [39]. This empirical criterion has been most useful [8] in identifying glass-forming compositions in various alloy systems.

2.4 Joining Behaviour

From the joining point of view, maintenance of BMGs in their amorphous state is important in keeping their unique physical, mechanical and chemical properties. Any joining process needs to prevent crystallisation of the BMGs, e.g. by joining at temperatures below the crystallisation temperature (T_x) of the BMG. Welding processes, even solid-state ones, tend to require elevated temperatures exposure that is likely to exceed the crystallisation temperature of the BMG. Crystallisation of the BMG in the bulk or interfacial zones during joining embrittles them and can reduce thir hardness. BMGs in several systems have been successfully welded together as supercooled liquid phase [40] welding using friction method [41], electron beam [42], explosive, pulse and laser welding [43-44].

CHAPTER 3 BRAZING

Brazing is a joining method that uses a molten interlayer without melting of the substrate, and so is similar to soldering. However, braze interlayers have higher melting temperatures relative to that of the substrate than solders so that greater amounts of interdiffusion between the braze and the substrate occur. This leads to greater chemical bonding across the bond-line and so greater bond strength.

The advantages of brazing are that strong, uniform, leak-proof joints can be made rapidly without melting of the substrate, reducing distortion and microstructural modification; this should allow brazes to join BMGs below their crystallisation temperature (T_x).

3.1 Mechanism

Brazing and soldering have similar mechanisms for joining, which involves melting of an interlayer whilst the substrate remains fully solid. Thus the interlayer liquidus temperature must be below the solidus temperature(s) of the base metal (below crystalline temperature (T_x) for BMGs in this study). The main difference is that brazing temperatures are much higher than soldering temperature. For successful joining, the molten filler metal must be held in the joint by surface tension; spread into the joint; and wet the base metal surfaces. On cooling and solidification of the interlayer, capillary action holding the liquid in the joint is replaced by metallurgical reaction and atomic bonding [45].

3.2 Phenomena Involved in Brazing

Capillary flow is the physical phenomenon that ensures joining by brazing. The molten filler metal must wet the faying surfaces to permit efficient capillary action and coalescence with substrate. Brazability can also be influenced by factors such as fluidity,

viscosity and vapor pressure of the filler metal; gravity; and any metallurgical reactions between the filler metal and the substrate.

Wettability is very important to the formation of brazed joints. High wettability means the thermocapillary attraction that fills the braze joint is strong [45]. The condition for wetting, experimentally determined, is shown in Figure 4 [46]. γ_{lv}, the liquid-vapor surface tension, γ_{sl} , the solid-liquid surface tension, γ_{sv}, the solid-vapor surface tension, θ the contact angle between the solid and the liquid is defined in equilibrium condition. The relationship between the contact angle and the surface tensions is given by the Young-Dupre equation, Equation 3-1 [47]:

Equation 3-1

$$\gamma_{lv} \cdot \cos\theta = \gamma_{sv} - \gamma_{sl}$$

Where $\gamma_{lv} \cdot \cos\theta$ is the resistive force that opposes a liquid wetting a solid. $\gamma_{sv} - \gamma_{sl}$ is the driving force for wetting. If the resistive force, $(\gamma_{lv} \cdot \cos\theta)$, is greater than the driving force for wetting $(\gamma_{sv} - \gamma_{sl})$, then no wetting will occur. It is important to decrease the resistive force and/or to increase the driving force for wetting.

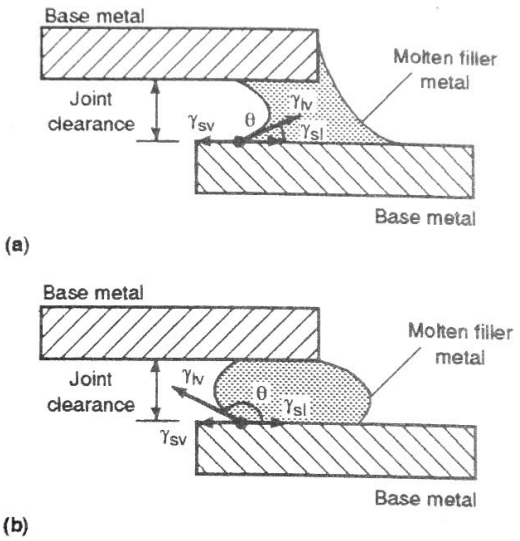

Figure 4 Schematic diagram illustrating the relationship of contact angle between liquid filler (brazing) metal and substrate [46].

3.3 Interfacial Reactions

During brazing, the molten filler metal often reacts with the base metal. When an interfacial reaction occurs between the base metal and the liquid filler, the free energy of the reaction per unit area ΔG_r should be included in equation 3-1:

Equation 3-2

$$\gamma_{sv} - \left(\gamma'_{sl} - \Delta G_r\right) = \gamma_{lv} \cdot \cos\theta$$

When a chemical reaction occurs, γ'_{sl} is smaller than γ_{sl}. The variables γ'_{sl} and ΔG_r will increase the driving force for wetting. If the driving force is greater than $\gamma_{lv} \cdot \cos\theta$, spreading will occur until the liquid has reacted completely with the solid surface.

Under equilibrium conditions, phase diagrams are good tools to estimate the compatibility between the filler and the base metal. Equilibrium phase diagrams will show any eutectic compositions, which will have the lowest fluid viscosity. Most brazing filler metals contain more than two elements and their phase relationships are more complex than shown in binary phase diagrams.

3.4 Activation Energy

The activation energy is defined as the minimum excess free energy that reactants must have in order to form products (phases), as shown in Figure 5 [48]. It can be related to reaction / transformation rates through the Arrhenius equation, Equation 3-3.

Equation 3-3 [48]

$$k = k_0 \exp\left(\frac{-Q}{RT}\right)$$

Where k and Q are the temperature-sensitive factor and activation energy at a given time. The parameter k_0 is a constant. R and T are the universal gas constant and absolute temperature.

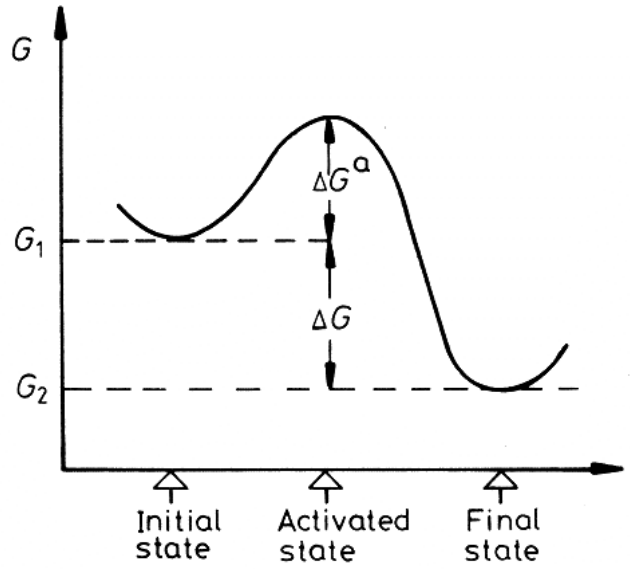

Figure 5 Schematic diagram illustrating the potential energy profile for an exothermic reaction. The energy barrier (ΔG^a is also referred to as Q) [49].

3.5 Diffusion and Dissolution

In the presence of the liquid braze alloy, base metal dissolution and solid-state diffusion can occur. Depending on the inter-solubility of the braze alloy and base metal, alloying element atoms in the filler metal may transmigrate into the substrate through solid-state diffusion or liquid metal grain boundary penetration; in addition, the base metal elements possibly diffuse into the interlayer.

3.5.1 Diffusion in Zirconium and Amorphous Zr-Based Alloys During Brazing

In brazing, diffusion is an important mechanism, by which metallurgical reactions and bonding between the filler metal and base metal are achieved. Diffusion is an irreversible process and is represented by the flux of atoms, J, crossing unit area in unit time. Steady state diffusion (under a constant activity or concentration gradient) is governed by Fick's first law, Equation 3-4.

Equation 3-4 [50]

$$J = -D\,\nabla C$$

where ∇C is the Laplacian of C, the gradient of concentration, (it is illustrated in different coordinate systems by Crank [50]) and D (m^2/s) is the diffusion coefficient.

In any system, diffusion can occur either through the bulk of the crystal as volume or lattice diffusion or along grain boundaries or dislocations (pipe diffusion). In an early study, Kijek [51] pointed out that, in amorphous alloys, there is a distribution in sizes of interstitial cavities, but that these are very similar to the interstice size in an equivalent close-packed crystal [52]. This is also evidenced by the similar densities of amorphous and crystalline structures of the same alloy [27]. However, the rate of interstitial diffusion is different in amorphous and crystalline structures even for the same alloy, the diffusivity of Zr-based bulk metallic glasses is smaller than that of α-Zr (hcp) crystal because diffusing atoms can be trapped at the larger interstitial sites [15], e.g. diffusion coefficients for Fe diffusion in Vitreloy 4 and single-crystal α-Zr at 600 K are approximately 10^{-19} and 10^{-12} (m^2s^{-1}) [28][53]. In addition, the diffusivities of several elements that diffuse in Vitreloy 4 exhibit a nonlinear Arrhenius behaviour as shown in Figure 6. BMGs have been reported to follow the linear Arrhenius behaviour within experimental accuracy in the supercooled liquid state. [53-55].

Diffusion in metallic glasses has been recently studied [57-58] as a fundamental process to control the GFA, thermal stability and viscosity. Diffusion in metallic glasses can exhibit either nonlinear or linear Arrhenius behaviour in different temperature regimes. The bond strengths, size of diffusing elements and the effective amount of the base metal element influence the activation energy (Q) [57]. Non-linear Arrhenius behaviour would suggest that more than one process is taking place with a range of different activation energies; this would be consistent with a range of interstice sizes in the amorphous material so that diffusion involving the larger ones occurs with little strain and so low activation energy. Increased temperature would allow the smaller interstices to be involved, but these require different strain energies and so would exhibit a different activation energy, thus a range of activation energies would be possible depending on diffusion temperature and a change from linear to nonlinear Arrhenius behaviour with temperature would be expected.

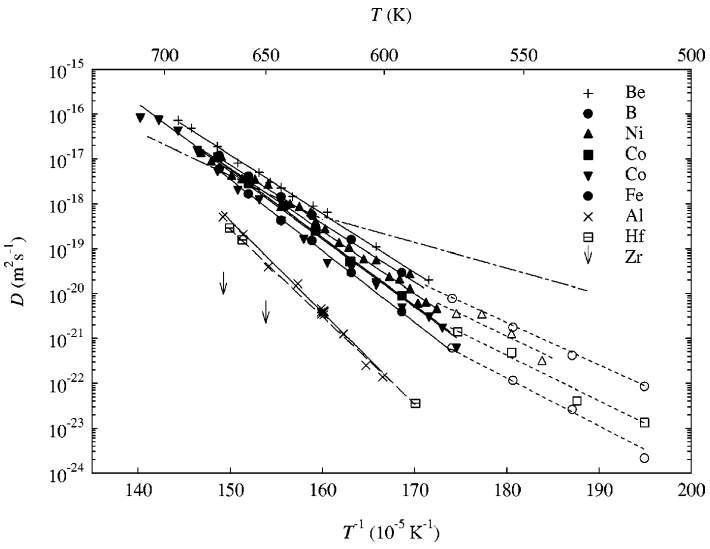

Figure 6 Arrhenius diagram for tracer diffusion in Vitreloy 4. The dashed-dotted line represents interdiffusion data obtained from Be-Vitreloy 4 diffusion couples [53].

CHAPTER 4 BRAZING ALLOY SELECTION

Several studies show that joining one BMG to another or a BMG to a crystalline metal using joining technologies such as electron beam welding, friction welding and soldering can improve the workability of BMGs. These approaches help offset the limitation of BMGs in terms of size for engineering and structural applications whilst maintaining their unique properties [41-42][59-61].

To maintain the beneficial properties of Vitreloy 105, crystallisation during joining must be avoided. Therefore, a brazing technique has been chosen for joining Vitreloy 105 plates. The general lack of reports on experimental studies into brazing of BMGs and the time-consuming nature of empirical approaches mean that this study will investigate the mechanisms occurring for brazing of crystalline Zr to itself using braze alloys developed for the similar titanium-based system, e.g. Cusil ABA. Once the interactions for braze alloy and crystalline Zr have been determined, confirmatory tests using Vitreloy 105 will be carried out.

CHAPTER 5 EXPERIMENTAL METHODS

5.1 Prediction of Filler – Substrate Interaction

The prediction is based on the software program, Thermo-Calc, which was used to calculate the amount and composition of stable phases as a function of composition, temperature and pressure. The input temperature was used 1213 K (940 ^{o}C), which was calculated with Version R of Thermo-Calc with SSOL-2 database, as the liquidus temperature of Cusil ABA. At 940 ^{o}C the stability of different mixes of filler and base material (from pure substrate to pure braze, e.g. 10% braze, 90% Zr and 20% braze, 80% Zr etc.) was determined. This was used to determine the composition range and end compositions for single and multiple phase regions from the braze alloy into the substrate. The greater the composition difference between the end members then the greater the likely interdiffusion and so these parameters should relate to greater wettability and brazed joint strength. However, the formation of complex multi-phase equilibrium structures could limit interaction and embrittle the joint region; this was taken as a measure that the proposed brazing system was not suitable.

5.2 Sample Preparation

Initial substrate samples (pure zirconium plates) 3 mm in thickness were cut from 16 mm diameter zirconium bar (99.94 at. % purity) using a diamond wafering blade on a Struers Minitom slow speed saw at 150 rpm. These were used for wettability experiments. Wire electrical discharge machine (WEDM) technique was used for cutting of brazing experiment work. 2500 grade SiC paper was used to remove the oxide layer. Vitreloy 105 ingots (3 mm in diameter and 50 mm in length) were prepared by copper mould suction-casting in an argon atmosphere [14]. Thermal properties had been measured using differential scanning

calorimetry (DSC) with a heating rate of 0.33 K/s; the glass transition temperature T_g, the crystallisation temperature T_x were 691 K and 753 K.

0.13 mm thick Cusil ABA ($Ag_{63}Cu_{35.25}Ti_{1.75}$) brazing foil was purchased from VBC group. 3 mm diameter circular coupons were punched from the foil for wettability trials or were cut into same size as substrate (16 mm diameter) for brazing trials. Both, filler metal and substrates were ultrasonically cleaned in ethanol for 120 seconds before each experiment.

5.3 Wettability Experiments

The 3 mm diameter discs of Cusil ABA ($Ag_{63}Cu_{35.25}Ti_{1.75}$) foil were placed at the centre of a 16 mm quadrant of zirconium plate as shown in Figure 7, which shows specimens after wettability experiments. The samples were held in the furnace at a temperature of 940 ^{o}C for different time between 1 and 10 minutes, Table 4, in air. The furnace was heated up to 940 ^{o}C before each specimen was inserted. The start of the hold time was taken when the substrate reached 940. A K-type thermocouple was used to measure the substrate temperature directly; on completion of the hold time the sample was removed from the furnace and left to cool in air.

Table 4 Cusil ABA – Zr wettability trial parameters

Specimen	Temperature (^{o}C)	T (min.)
S1	940	1
S2	940	2
S3	940	3
S4	940	5
S5	940	10

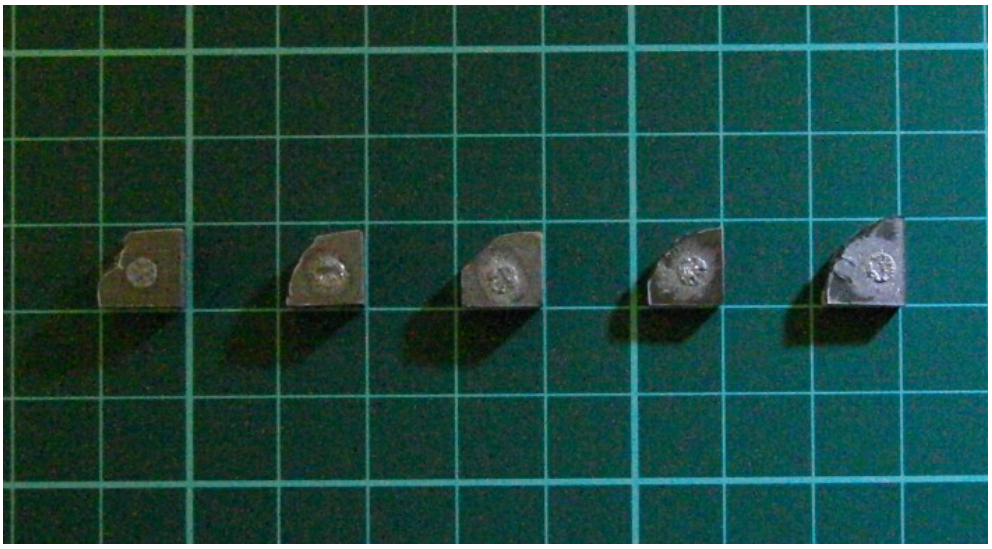

Figure 7 Wettability samples after furnace holding showing spreading of braze alloy on the crystalline pure Zr plate from the original 3 mm diameter discs of Cusil ABA brazing alloy (S1 to S5 from left to right).

5.4 Brazing Trials

Brazing trials were carried out at 3 different temperatures (60, 120 and 180 ^{o}C above the melting temperature of Cusil ABA, for various isothermal holding times between 1 and 10 min., Table 5.

Each specimen, composed of a brazing alloy disc placed between two substrate discs, was held between the compression grips of a Gleeble 3500 thermo-mechanical simulator. The chamber was pumped down to 2.6 x 10^{-1} torr and flushed with pure argon (Ar) gas (purity >99.9%) to 6.8 x 10^{0} torr 3 times to minimise the residual oxygen content of the specimen chamber. The heating and cooling rates used were 5 K/s.

5.5 Microstructural and Mechanical Property Analysis

Sections transverse to the joint plane were cut using a Struers Minitom slow speed saw with a diamond wafering blade operated at 150 rpm. The freshly cut sections were hot mounted in bakelite at 170 ^{o}C for 2 minutes. Each specimen was ground and polished from

800 grade SiC paper to 4000 grade SiC paper and finished with OP-S (grain size of 0.04 μm) on a MD-Chem pad, as shown in Table 6.

5.5.1 Microstructural Analysis

Microstructural and composition analyses were carried out using a JEOL-6060 SEM-EDS and a JEOL JXA-8900R EPMA operating at 15 kV. Wavelength dispersive X-ray spectroscopy (WDS) mapping was used to determine elemental redistibution by diffusion during brazing.

5.5.2 X-ray Diffraction (XRD)

XRD specimens were cut across the joint at an angle of 10° to increase the area of the joint exposed to the incident Cu K_α X-rays. The exposed surface of the specimens was polished with wet 2500 grade SiC paper, and subsequently cleaned in ethanol using an ultrasonic bath before XRD.

The data were collected 2θ data, which every 0.05 degree per second, from 20-100° by using a Bruker D8 Advance diffractometer.

5.5.3 Microhardness Testing

Microhardness tests were carried out under 50 grams load, held for 5 seconds using a Vickers diamond indenter with Shimadzu HMV-2000 tester. As shown in figure 8, the indents were measured on the cross-sections of sandwich structures (e.g. substrate, interlayer, substrate). In order to increase spatial resolution indents were separated vertically (normal to the joint plane) about 35 μm vertically and about 100 μm horizontal (parallel to the joint).

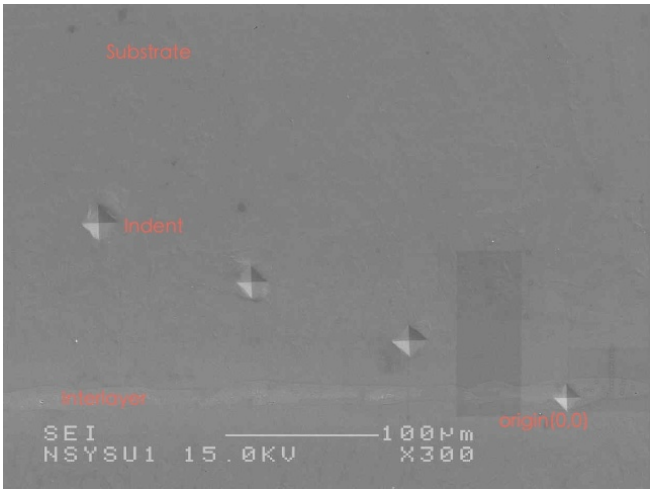

Figure 8 S3GV cross section of Vickers microhardness indent.

5.5.4 Shear Testing

To evaluate the bond strength of the joints, shear tests were performed using an Instron 5582 universal tester in compression. The specimens were cut into 16mm diameter semicircles and placed in the clamping apparatus for loading as shown in figure 9. A constant deformation rate of 0.05 mm per second was used.

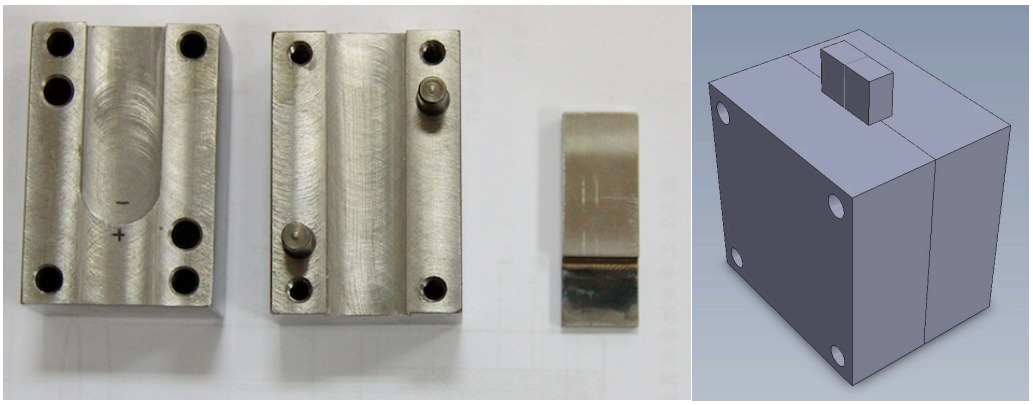

Figure 9 Shear test performed in compression mold

Table 5 Brazing conditions of Zr and Vitreloy 105 brazed with Cusil ABA in the Gleeble 3500

Gleeble vacuum		
Cusil ABA- Zr		
	Temperature (°C)	Time (min.)
S1GVA	880	1
S2GVA	880	2
S3GVA	880	3
S4GVA	880	5
S5GVA	880	10
	Temperature (°C)	Time (min.)
S1GV	940	1
S2GV	940	2
S3GV	940	3
S4GV	940	5
S5GV	940	10
	Temperature (°C)	Time (min.)
S1GVB	1000	1
Cusil ABA-Vitreloy105		
	Temperature (°C)	Time (min.)
VIT105	780	1

Table 6 Preparation of the cross-section surface for microstructural analysis

Polish order	Surface	Lubricant/Abrasive	Time (min.)
800	SiC grit paper	water	-
1500	SiC grit paper	water	3
2500	SiC grit paper	water	3
4000	SiC grit paper	water	3
OP-S	MD-Chem	OP-S	10

CHAPTER 6 RESULTS AND DISCUSSION

6.1 Prediction of Cusil ABA Active Braze Alloy Interaction with Pure Zirconium.

Thermo-Calc prediction has been carried out for different starting mixes of braze and substrate and so represents equilibria from pure braze to pure substrate (without changing composition ratios within each). Figure 10 shows the predicted phase balance at 940 °C from pure Zr (bcc) to pure braze (liquid); Figure 11 shows the predicted composition variation through the interaction volume. For good brazing behaviour, the joint should exhibit a partially melted region where interdiffusion of Zr, Ag and Cu would occur. The solid phase in the partially melted region is predicted to be hcp, which is retained as a single phase through the interdiffusion zone as Zr increases at the expense of Ag and Cu, eventually giving a narrow (bcc + hcp) two phase region. In terms of brazing this is a desirable situation as interdiffusion is controlled by diffusion through the hcp phase and a single phase gives uniform interaction along the joint line. The main concern would be transformation and volume changes during post-brazing cooling, however, this would be minimised by having a uniform thickness interdiffusion zone.

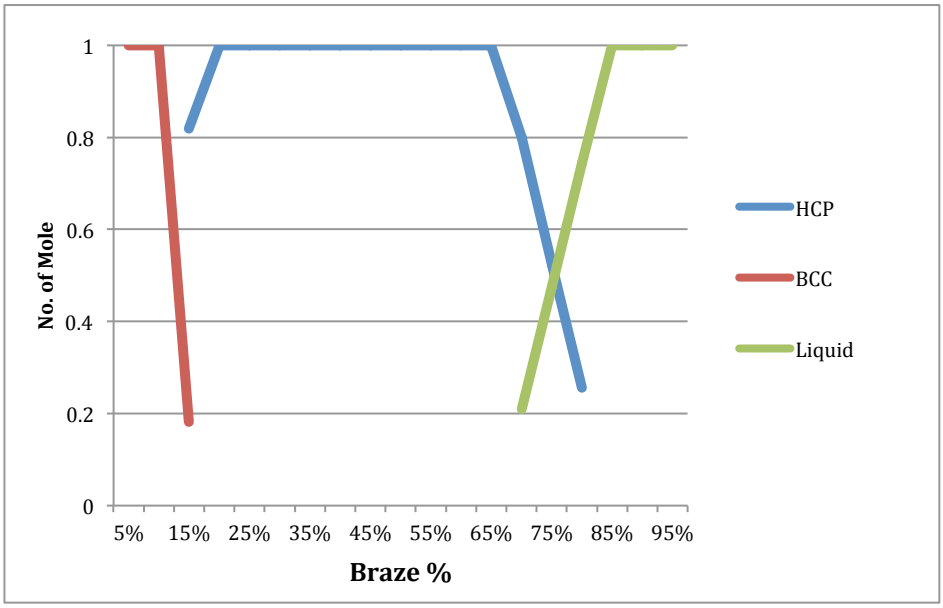

Figure 10 Predicted phase balance of mixtures of Cusil ABA with Zr at 1213 K (940 °C) from substrate (left) to molten Cusil ABA (right).

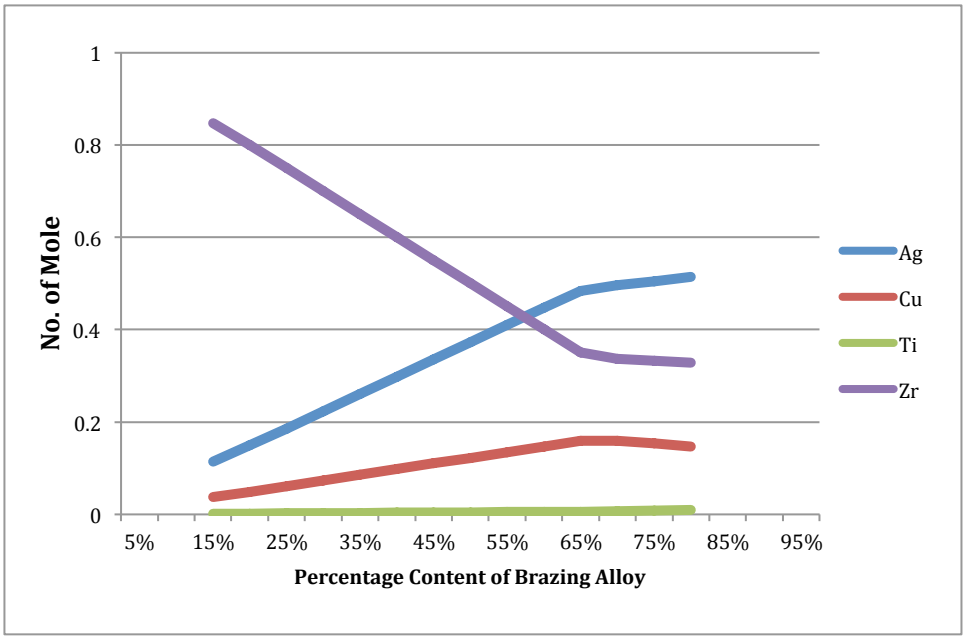

Figure 11 Predicted composition variation in mainly hcp phase from substrate (left) to molten brazing alloy (right) at 1213 K.

6.2 Wettability Trials of Zr by Cusil ABA

6.2.1 Microstructural Analysis

Wettability of Zr by Cusil ABA ($Ag_{63}Cu_{35.25}Ti_{1.75}$) is expected to increase with time from the prediction of single-phase interdiffusion (Section 6.1). Wetting was characterised by the final braze coupon area (the original area was constant). The variation in this parameter, Figure 12, shows a linear variation with ln(time), i.e. a parabolic variation in radius with time. This would be consistent with spreading being controlled by a diffusion process. Sectioning through the braze coupon and substrate, Figure 13, shows a multiple layer structure to the interaction zone. As an air atmosphere was used in the furnace, the structures differed from those predicted by Thermo-Calc, with a zirconia (ZrO_2) layer, which was identified by XRD as shown in Figure 14, at the interface between the braze and the substrate underlain by oxygen diffusion into zirconium (Zr(O)). Figure 15 shows the thickness of the oxygen diffusion zone is relatively constant with increasing brazing time, suggesting that this process has saturated early with any further diffusion not providing oxygen for further diffusion into the substrate. The ZrO_2 layer increases in thickness and the oxygen diffusion layer has a consistent constant thickness with increased holding time. Under the braze zone, ZrO_2 layer can be thicker than non-braze zone; on the contrary, the oxygen diffusion layer is slightly thinner than non-braze zone. However, these differences mostly fall within the scatter of the experimental data.

After brazing, the braze alloy appeared to separate into two regions, copper-rich and silver-rich, Figure 16. The Cusil ABA ($Ag_{63}Cu_{35.25}Ti_{1.75}$) composition is silver-rich, but close to the eutectic point (Cu 39.9 at. % and Ag 60.1 at. %) in the binary phase diagram [62]. An interaction layer (about 20 μm thick) between the braze and the Zr substrate formed, which appeared to be composed of zirconia and an underlying oxygen-enriched diffusion zone.

Some cracks on the ZrO_2 layer are observed for longer holding times (greater than 3 minutes). This might be caused during preparation for microstructure analysis, i.e. cutting or polishing. The layer between the ZrO_2 and substrate is the solid solution of oxygen in zirconium, Zr(O), which is about 15 μm thick (Figure 17).

It should be noted that the contact surfaces between brazing alloy and substrate are not perfectly flat. Therefore, air easily gets into the liquid brazing alloy before dissolving into the zirconium. As calculated, the thicknesses of ZrO_2 layers, where air bubbles appear, are thicker (approximately 18%) than under the rest of the brazing zone, (Figure 17).

6.2.2 Microhardness

Figure 18 shows that the hardness of the two layers (ZrO_2 and solid solution layer of oxygen in Zr), the zirconium substrate and braze alloy. The hardness of ZrO_2 is decreased dramatically at the non-braze zone with increasing time. The zirconia layer hardness showed a variation between brazed and non-brazed regions after holding for 2 minutes or longer, but this was not consistent with the non-brazed region being harder at 2 minutes, but softer for longer times. The hardness of the Zr(O) layer was quite scattered and generally the data points fell within the scatterband so there appeared to be little difference in hardness between brazed and non-brazed regions. Both oxygen-rich layers were consistently harder than the base Zr. The Cusil ABA braze was consistently the softest region and showed no consistent trend with holding time, just a broad scatterband.

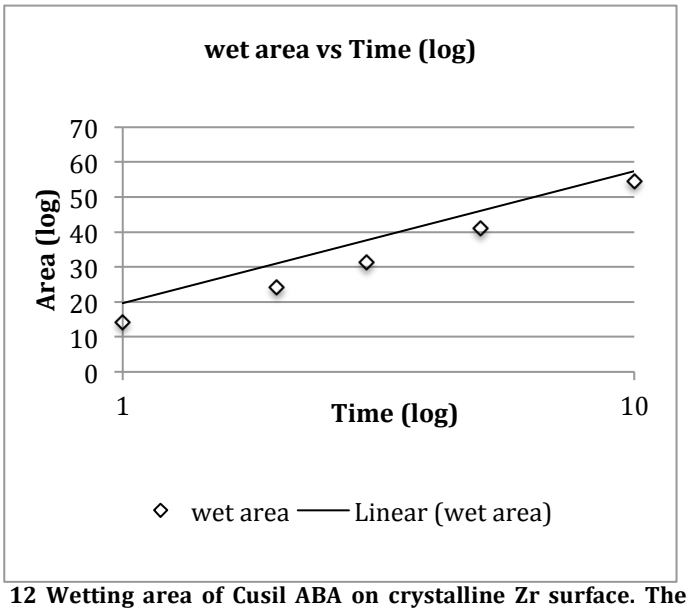

Figure 12 Wetting area of Cusil ABA on crystalline Zr surface. The trend line shows the ratio of original coupon area to heat-treated coupon area increasing with time.

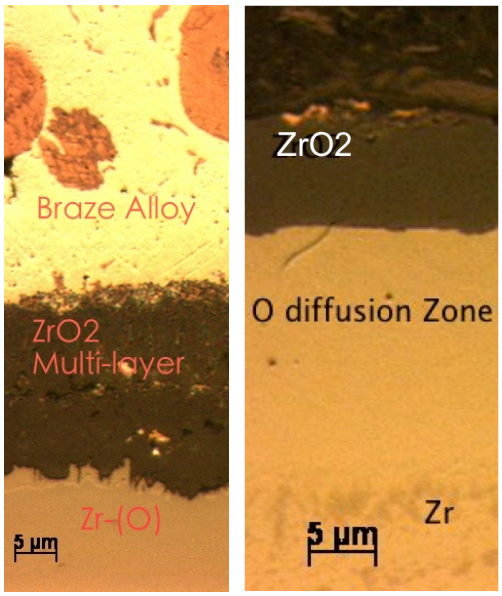

Figure 13 Cross-section of braze zone (left) and non-braze zone (right)

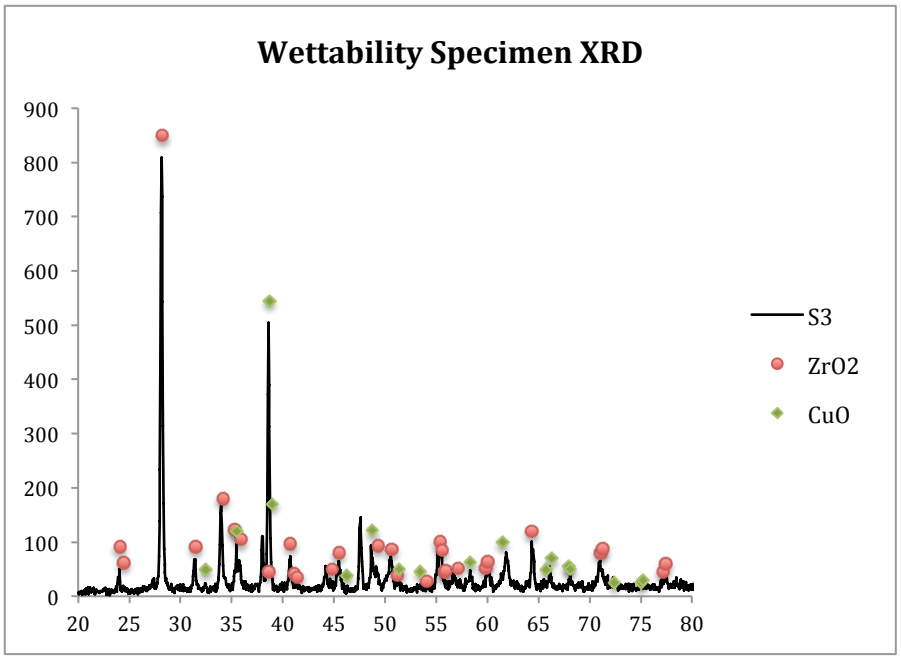

Figure 14 Wettability trails (S1-S5) has been identified the oxide of zirconium (ZrO_2) and copper (CuO) by XRD.

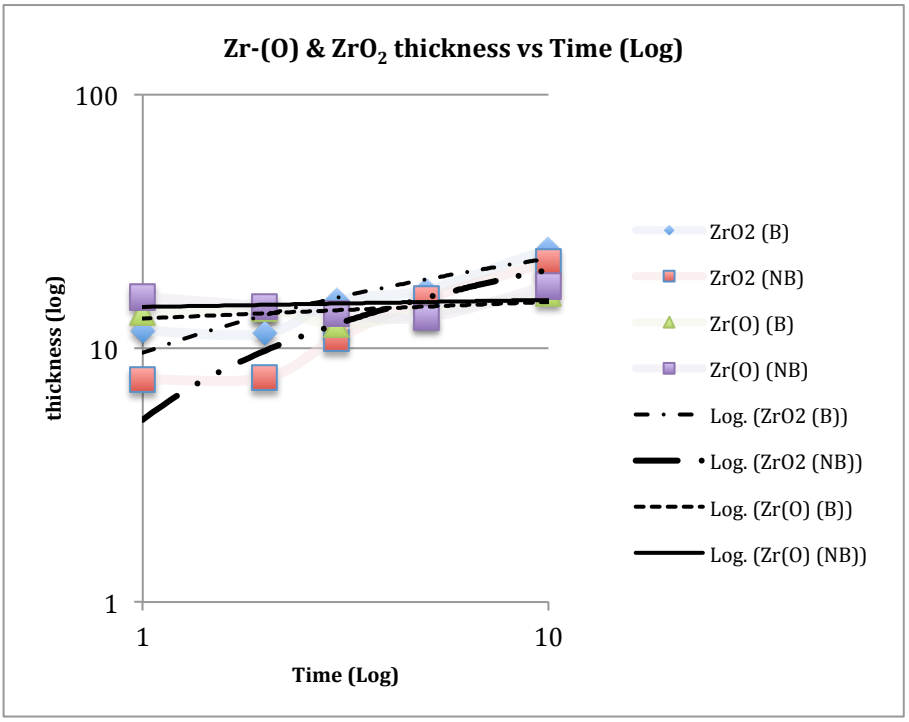

Figure 15 Thickness of zirconium oxide (ZrO_2) and solid solution oxygen in Zr layers (Zr(O)) against with logarithmic time

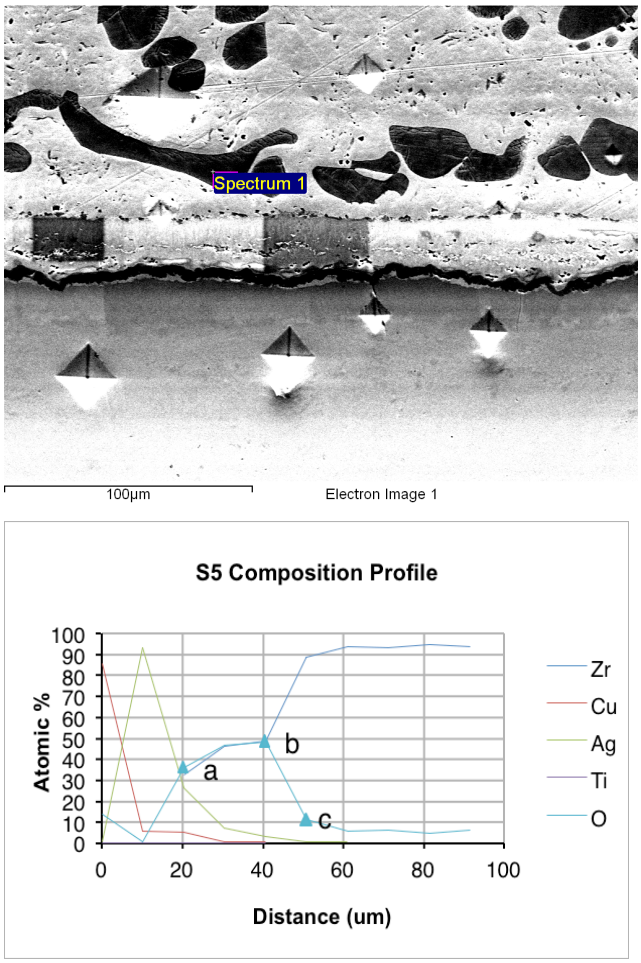

Figure 16 S5 image (top) and composition profile (bottom) was taken from SEM and EDS. The composition profile start from braze alloy at 0-20 µm, 20-40 µm is the reaction layer in between, to Zr substrate (50-90µm).

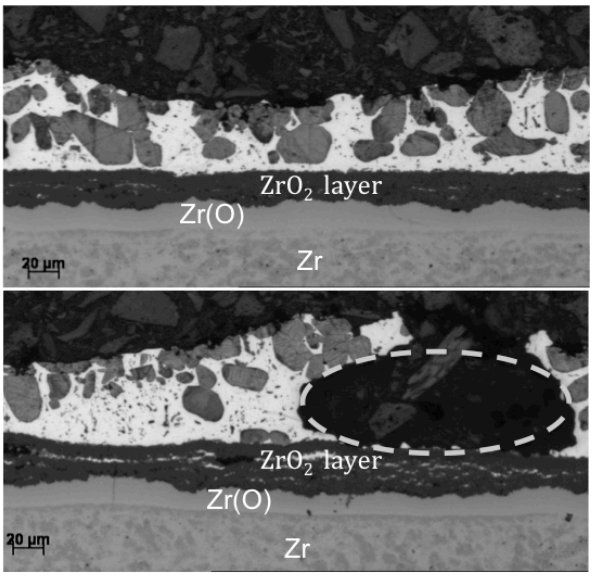

Figure 17 Different thickness of ZrO_2 layer under the braze zone (top) and air appear in the brazing area (dashed ellipse) after heat treatment (bottom).

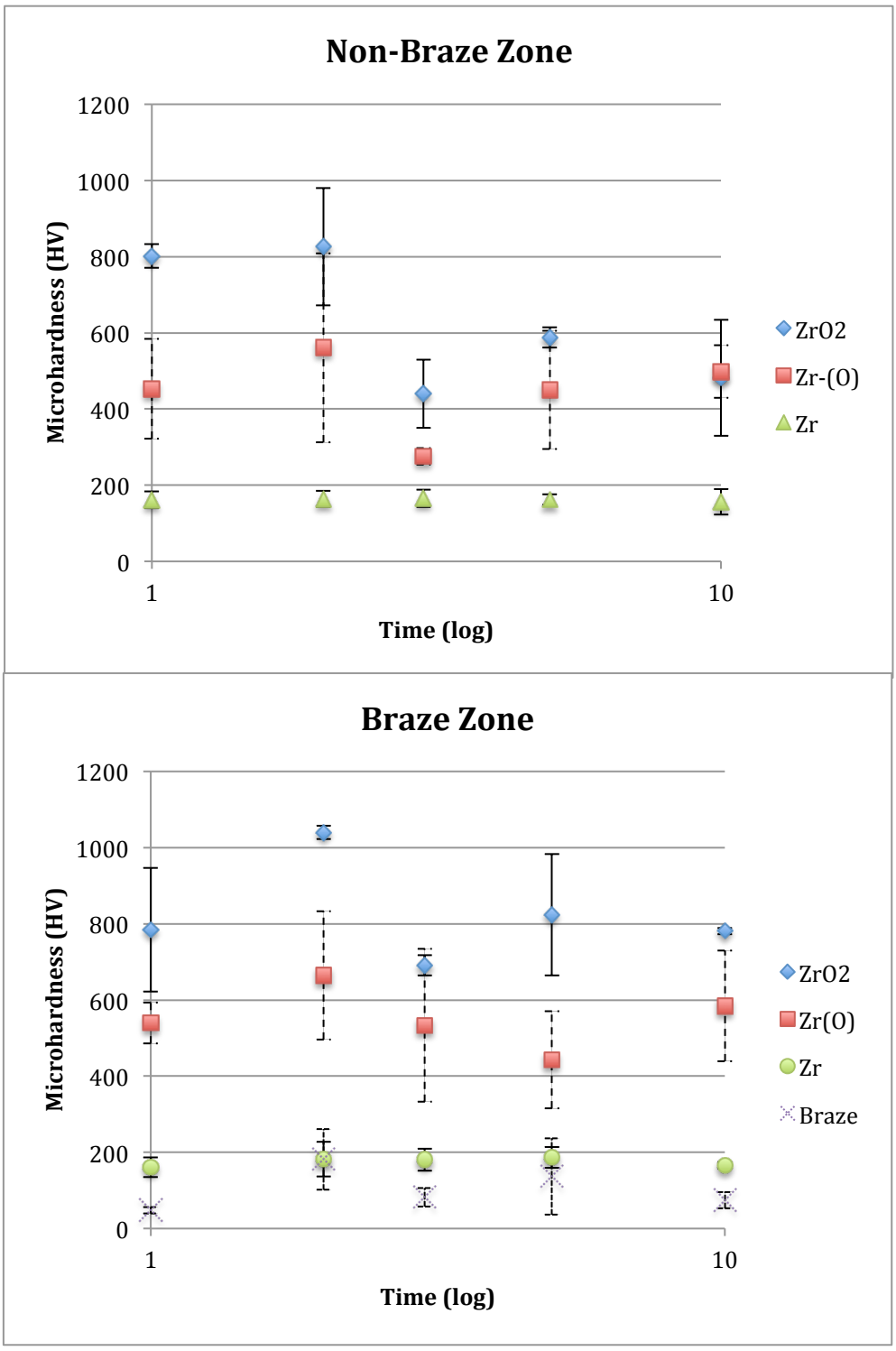

Figure 18 Hardness values (H_v 50g) of non-braze zone and braze zone as a function of time.

6.3 Discussion on Oxidation of Zirconium and its Alloys (Crystalline and Amorphous)

6.3.1 Oxidation in α-Zirconium

The solid solubility of oxygen in pure zirconium can be as high as 29.2 at. % [63]. The mechanism of oxygen dissolution in zirconium can be considered as occurring in two stages. Oxygen initially dissolves interstitially in α-Zr, α-Zr(O), up to its saturation limit with the formation of ZrO_2 [64][65]. The oxidation kinetics of crystalline zirconium could be described by cubic behaviour in the range of temperature 400-800 ^{o}C and parabolic relationship is obtained at higher oxidation temperature. Oxidation kinetics have been determined as being rate controlled by oxygen-diffusion in α-zirconium in many studies [66-69]. The oxygen diffusion coefficient, D, for jumps of the interstitial oxygen atom in the zirconium lattice is given for two temperatures ranges by Equation 6-1 and Equation 6-2.

$$D = 0.0661 \exp\left(-\frac{44000}{RT}\right) \qquad 290 < T \leq 650\ ^{o}C \qquad \text{(Equation 6-1)}$$

$$D = 16.5 \exp\left(-\frac{54700}{RT}\right) \qquad 650 < T < 1500\ ^{o}C \qquad \text{(Equation 6-2)}$$

In this study, the wettability experiments were carried out at 940 ^{o}C for 10 minutes or less. As Östhagen and Kofstad have pointed out at 800 ^{o}C for up to about 10 minutes, the rate of zirconium oxidation remained the same controlled by oxygen dissolved in the zirconium. Later stages of oxidation obeyed a cubic rate law [64][70]. While the wettability trial temperatures are above the α-β transition temperature of 862 ^{o}C, there are three stages of oxidation above this temperature. These three are (i) oxygen dissolving into the metal to stabilise the α-zirconium phase on cooling, (ii) formation of a surface oxide (ZrO_2) and (iii) intermediate formation of stabilised α-phase are formed in β-zirconium during oxidation. Accordingly, at temperatures where the parabolic law is observed for Zr oxidation, the growth

rate of the oxide is not just controlled by oxygen diffusion in zirconium, but also might be controlled by oxygen diffusion in the oxide. The ZrO_2 layer thickness (x) is proportional to the square root of time [71].

$$x^2 \propto t \qquad \text{(Equation 6-3)}$$

For a rough estimation of the diffusion coefficient of O in ZrO_2 (D_{ZrO_2} as shown in Table 7), Equation 6-3 can be written as

$$x^2 \cong D_{ZrO_2} t \qquad \text{(Equation 6-4)}$$

The result of wettability trials show that the thickness of the zirconia layer is consistent with equation 6-4 for $D_{0_{ZrO_2}}$ in the temperature range 875-1050 ^{o}C, as calculated and shown in Figure 19.

Table 7 Diffusion coefficients for oxygen in ZrO_2, $D_{ZrO_2} = D_{0_{ZrO_2}} \exp(-Q/RT)$

Temperature range (^{o}C)	$D_{0_{ZrO_2}}$ (cm^2/sec)	Q (kJ/mole)	Method of determination	Ref
400-800	1.05×10^{-3}	122.6	Moving boundary in oxide-metal system	[72]
700-1000	5.55×10^{-2}	139.8±12.98	Moving boundary in oxide-metal system	[73]
700-1000	1.1×10^{-3}	129.7±12.98		[74]
334-470	9.0×10^{-4}	120.14±2.51	Oxidation kinetics and interrupted-anneal technique.	[64]
875-1050	1.36×10^{-4}	118.88	Moving boundary in oxide-metal system	[75]

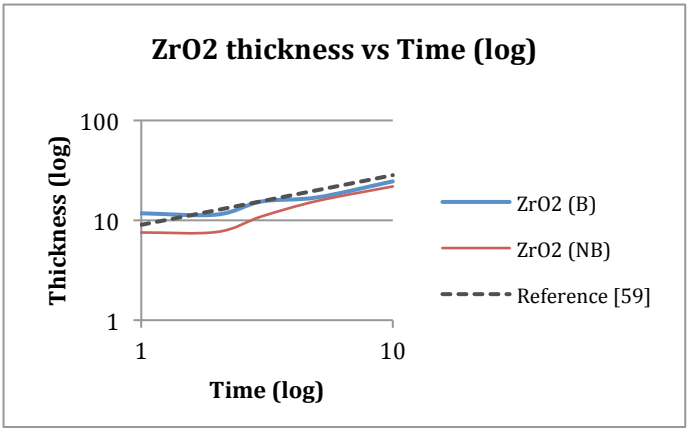

Figure 19 The thickness of zirconium oxide growth compared with Equation 6-4 in the temperature range 875-1050 ^{o}C.

6.3.2 Oxidation of Zr-based Crystalline Alloys and Bulk Metallic Glasses

Several investigations of oxidation kinetics of Zr-based metallic glasses show that oxidation behaviour is controlled by oxygen diffusion in Zr-based BMG and oxide growth follows a parabolic rate law (at 350-400 ^{o}C or higher temperature) and is linear at lower temperature (at 300 ^{o}C) [76-78]. The oxidation kinetics of $Zr_{53}Cu_{20}Ni_{12}Al_{10}Ti_5$, $Zr_{55}Cu_{30}Ni_5Al_{10}$, $Zr_{65}Cu_{15}Ni_{10}Al_{10}$ and $Zr_{58}Cu_{28}Al_{10}Ti_4$ were reported in air at various temperatures. The oxide scale formed consisted of a mixture of tetragonal and monoclinic-ZrO_2 and minor amounts of other alloying element oxides (CuO, NiO).

6.3.3 Oxidation Kinetics

Hsieh et al. [76] showed that the oxidation of $Zr_{53}Cu_{20}Ni_{12}Al_{10}Ti_5$ follows linear kinetics at T $\leq$ 350 ^{o}C and $Zr_{55}Cu_{30}Ni_5Al_{10}$ and $Zr_{65}Cu_{15}Ni_{10}Al_{10}$were also observed to exhibit linear kinetics at 300 ^{o}C. At higher temperatures, parabolic rate law behaviour was observed for these three BMGs, as well as for $Zr_{53}Cu_{20}Ni_{12}Al_{10}Ti_5$ at T > 350 ^{o}C and for $Zr_{65}Cu_{15}Ni_{10}Al_{10}$ at T $\geq$ 300 ^{o}C. The oxidation kinetics of BMGs do not follow a simple Arrhenius equation. Solid-state diffusion of oxygen in BMG was the rate-limiting step for parabolic growth at T >350 ^{o}C. The oxidation rate constants (K_p) for BMGs fluctuate with increasing temperature as shown in Table 8. It should be noted that amorphous alloys initially have a faster oxidation rate than the rate in crystalline zirconium below the glass temperature T_g, but exhibited a slower rate at temperatures above T_g.

The oxidation kinetics of BMG and crystalline alloys of $Zr_{55}Cu_{30}Ni_5Al_{10}$ were investigated by Kai et al. [79]. That study showed that the oxidation rates for the amorphous alloy are slightly higher than for the crystalline alloy at 350 - 400 ^{o}C but lower at 425 ^{o}C (T_g = 400 ^{o}C)

Table 8 Oxidation rate constant, K_p ($g^2/cm^4/s$) of Zr-based BMGs, crystalline alloy and pure zirconium at 300-500 ^oC (Zr53: $Zr_{53}Cu_{20}Ni_{12}Al_{10}Ti_5$, T_g=384 ^oC; Zr55: $Zr_{55}Cu_{30}Ni_5Al_{10}$, T_g=400 ^oC; Zr65: $Zr_{65}Cu_{15}Ni_{10}Al_{10}$, Tg=368 ^oC)

Temperature (^oC)	Zr53	Zr55	Zr65	Zr55 crystalline	Pure Zr
300	linear	linear	linear	3.77E-13	
350	linear	1.16E-11	1.05E-11	2.34E-12	
375	4.82E-11	2.06E-11	1.39E-12	8.18E-12	
400	6.61E-11	8.76E-12	2.62E-12	8.82E-12	2.90E-13
425	1.54E-10	3.65E-12	2.02E-12		
450	1.44E-10	8.08E-13	1.59E-12		
500	4.80E-12	4.21E-13			1.80E-12
Ref.	[76]	[76]	[76]	[79]	[80]

6.4 Brazing of Zr Using Cusil ABA

6.4.1 Microstructure of Joints

The microstructures of samples brazed at three different temperatures exhibited similar interactions between the substrate materials. As wettability trials were carried out in air, zirconia was formed between the substrate and brazing foil. The Cusil-ABA brazing foil wetted the zirconia surface and reacted with zirconium. This might cause differences between the wettability trail results and those of the braze simulations as the latter were carried out under vacuum. Figure 20 shows the SEM images of the multi-phase interfacial region for brazing simulations at 880 ^{o}C (S1GVA) and 940 ^{o}C (S1GV) for 1 min. The Ag-Cu eutectic active braze alloy with Ti addition reacted with the Zr substrate. The microstructure of the brazed region mainly consisted of Ag-rich, Cu-rich and Zr-Cu-Ag phases, which constitute the reaction layer. SEM-EPMA, Figure 22, observations revealed that the Cu-rich phase has a stronger affinity for zirconium; the Ag-rich phase is not in contact with the substrate during brazing. The reaction layer is Zr alloyed with Cu and Ag, which is formed as the molten Cusil-ABA at the brazing temperature react with solid Zr. In addition, alloying elements from liquid Cusil-ABA enter the solid Zr and then diffuse through the solid Zr away from the original substrate surface. The result shows that brazing time or temperature increased, the brazed region tended to become more uniform, forming bands, as Figure 20 shows. The mapping measurements from SEM-EPMA, Figure 24-27, demonstrate the effect of time from 1 to 10 minutes at 940 ^{o}C. The results of EPMA mapping (Figure 24-27) shows that each element is distributed between substrate and joint. There is a zone of solid state diffusion, where copper, silver and titanium diffused or dissolved into the zirconium. Also shown is the greater diffusion of copper into zirconium then silver, where diffusion coefficient of Cu is 40 times larger than that of Ag in Zr at temperatures above α-β transition temperature [81]. Note

that no oxidation occurred in the jointed region (between the braze alloy and substrates) compared to the wettability trials, as shown in Figures 16 and 22. This result shows that no air (oxygen) remained between the braze and the substrate due to the vacuum conditions and compression loading. The vacuum in the Gleeble was not complete leading to limited oxidation at both edges of the joint, however, the molten brazing alloy prevented oxygen entering the substrate under the brazing area. The composition of joint is formed with liquid Cusil ABA dissolving into the zirconium.

6.4.2 Interfacial Reactions

The chemical composition of the Cusil-ABA in atomic percent is 49.7Ag-47.2Cu-3.1Ti. The liquidus temperature of the Cusil-ABA alloy is 815 ^{o}C, which can form a homogeneous liquid at brazing temperatures over 840 ºC. The molten Cusil-ABA reacted with the zirconium substrate. The result of EPMA for joint compositions trace marker from brazed region to substrate as marked on Figure 22 and average composition of 3 phases in the brazed region are listed in Table 9. Three phases are (A) an AgZr phase (Ag-rich) containing approximately (39.3-52.2 at. %) of Ag, depending on the temperature and time, higher temperature and longer time gives greater reaction between Cusil ABA and Zr reducing the Ag content, and increasing that of Cu (B) a Cu-rich phase ($Cu_{10}Zr_7$+Cu_8Zr_3) is only observed in 880 ^{o}C containing 39 at. % Zr and small amounts of Ag and Ti. (C) a reaction layer, Zr-Cu-Ag phase, consists of over half atomic % of Zr (56-66 at. %), a quarter of Cu (15-27 at %), less than a fifth of Ag (20 at%) and the rest Ti. As a result of analysis of the reaction phase, its composition was determined to be $Zr_{56.1}Ag_{19.6}Cu_{22.6}Ti_{1.7}$ at 880 ^{o}C and $Zr_{65.1}Ag_{19.4}Cu_{13.9}Ti_{1.6}$ at 940 ^{o}C, with [Cu] decreasing for higher temperature and longer holding time. Ignoring the small amounts of Ti, there are a number of compounds following the cooling path of the

molten braze that might be found in the Zr-Cu-Ag ternary phase diagram shown in Figure 23 [82]. The reaction scheme of Ag-rich, Cu-rich and reaction layer is listed below, Table 10:

Table 9 Average composition (at. %) of each phases (Ag-, Cu-rich and reaction layer) in 2 different Temperatures systems. The trace marks are shown in Figure 18 (left) S1GV as an example.

Average Composition (at. %)			
Phase		940°C	880°C
A	Ag-rich	$Ag_{52.2}Zr_{38.4}Cu_{8.98}Ti_{0.42}$	$Ag_{46.4}Zr_{38.6}Cu_{13.8}Ti_{1.2}$ (1-2 min)
		$Ag_{41.8}Zr_{50}Cu_{7.15}Ti_{1.02}$	$Ag_{39.3}Zr_{39.2}Cu_{19.25}Ti_{2.25}$ (3-5 min)
B	Cu-rich	–	$Cu_{53.3}Zr_{39.45}Ag_{5.17}Ti_{2.05}$
C	Reaction layer	$Zr_{55.3}Ag_{28.97}Cu_{14.87}Ti_{0.86}$ (1min)	$Zr_{56.1}Ag_{19.6}Cu_{22.6}Ti_{1.7}$
		$Zr_{65.1}Ag_{19.4}Cu_{13.9}Ti_{1.6}$	

Table 10 The reaction scheme of Ag-rich, Cu-rich and reaction layer

Reaction	**Composition (at%)**	**Temp.(^oC)**	**References.**
$\text{Liq} \leftrightarrow \text{fcc(Cu)} + \text{fcc(Ag)}$	X(Ag)=0.599	780	[82]
$\text{Liq} \leftrightarrow \text{fcc(Ag)} + \text{AgZr}$	X(Zr)=0.056	940	[83]
$\text{Liq} \leftrightarrow \text{CuZr} + \text{CuZr}_2$	X(Zr)=0.435	912	[82]
$\text{iq} \rightarrow \text{AgZr} + (\text{Ag, Cu})\text{Zr}_2 + \text{CuZr}$	Liq*(12.88Ag-37.03Cu-41.99Zr)	882.2	[82]

*Liq, liquid composition of 12.88Ag-37.03Cu-41.99Zr.

6.4.3 Microhardness

Microhardness measurements were made at the joint interfaces using a Vickers microhardness test under a load of 50 g and loading time of 5 s. The Vickers microhardness profile was made approximately at an angle of 30 degree to the joint, as shown in Figure 28 (S3GV microstructure image). The results displayed a symmetrical pattern of value, from substrate through the joint to the other substrate. The joints centerlines were twice as hard as the base substrate, with the joint having a hardness of about H_v: 335±35. The values for the substrate and solid diffusion zone are about H_v: 180±10 and 230±30 respectively.

The hardness values (Hv: ~300-400) of the joint regions varied with brazing time for the three different conditions of SGVA (880 ^oC), SGV (940 ^oC) and SGVB (1000 ^oC). Figure 29 indicates time (log) against the value of microhardness for the three brazing temperatures. As thermal activation increased for the three difference temperatures (880, 940 and 1000 ^oC) for molten filler metal reacted with the substrates to a greater extent. The two extreme brazing temperatures have opposite behaviour, with SGVA joints exhibiting the phases, Cu-Zr ($Cu_{10}Zr_7 + Cu_8Zr_3$) and AgZr. Contrary to the result of SGV shows that the main phase of the joint is AgZr phase only. However the ultimate joint phase after 10 minutes holding for both systems approach the same level of hardness due to their compositions getting similar, as shown in Table 9. The rectangle in Figure 28 shows the Cu content. The EPMA result shows that the maximum solid dissolution of Cu in Zr is 5 at. % (Fig 22) and Ag is 3 at. %. From the Ag-Cu-Zr phase diagram, it was found $Zr+CuZr_2$ exists in this zone and increases the hardness.

6.4.4 Mechanical Behaviour (Shear Strength)

In order to assess the shear strengths of the joints of this plate sandwich structure, compression testing using the rig in Figure 9 was carried out. The results of the shear testing, Figure 30, indicated that the specimens brazed at 880 ^{o}C generally had higher shear strengths then samples brazed at 940 °C. For both brazing temperatures, holding for 1 or 5 minutes gave lower shear strengths than 2 – 4 minute holding times.

Table 11 shows that the mechanical properties (yield stress and Young's modulus) of substrate and Cusil ABA before brazing. An approximate Prandtl relationship between microhardness and yield stress under tension can be represented as $H/\sigma_y \approx 4.7$ for Zr [84].

The microhardness values of the joint and the matrix have averages of about Hv 300-370 and 170-190, therefore the yield stresses of the joint and the matrix are approximately 1010-1245 MPa and 360-404 MPa. Fractography and Energy Dispersive X-ray Spectroscopy (EDS) from the joint fracture surfaces (shown in Figures 31 and 32 and Tables 12 and 13) show differences between joints prepared using the 2 brazing temperatures. For a brazing temperature of 880 ^{o}C, Figure 32, the joint sheared through the interlayer close to the substrate (indicated by the elements present from the EDS traces) giving a smooth fracture appearance; on other hand, the joint was fractured through the substrate zirconium for brazing at a temperature of 940 ^{o}C , Figure 31, giving a much rougher appearance to the fracture surface. This would suggest that higher temperature brazing caused embrittlement of the braze – substrate interface (chemically and/or by stressing) that would help cause the large difference in shear strength values observed in Figure 30.

Table 11 Mechanical and physical properties of Cusil-ABA

Braze	E (GPa)	Hv	Yield stress, MPa	Reference
Cusil ABA	83	150	271	[85]
Zirconium	88	183-241	413.65	[84][86]

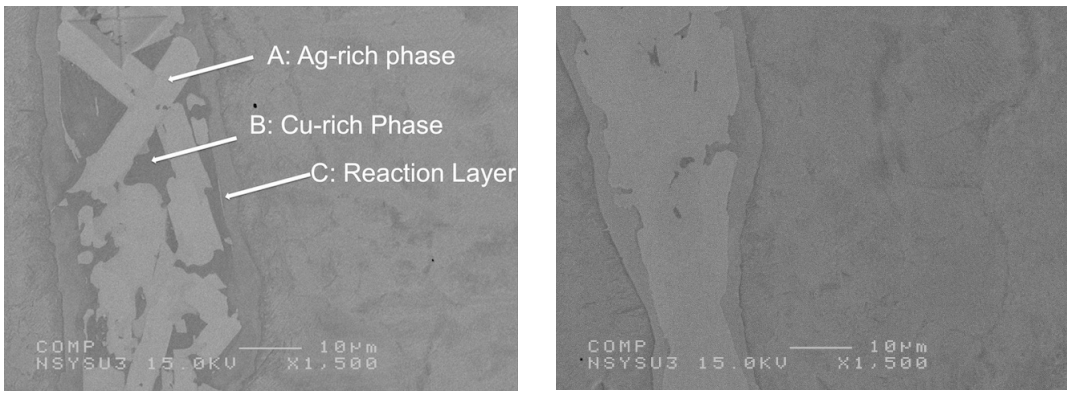

Figure 20 Cross-section of the multi-phases joint by SEM; S1GV, right, shows the even phase of the joint and the reaction layer between the joint and substrate and; S1GVA, left, shows the two phases in the joint, Cu-rich phase (dark gray, point A) and Ag-rich phase (light gray, point B) and reaction layer (point C).

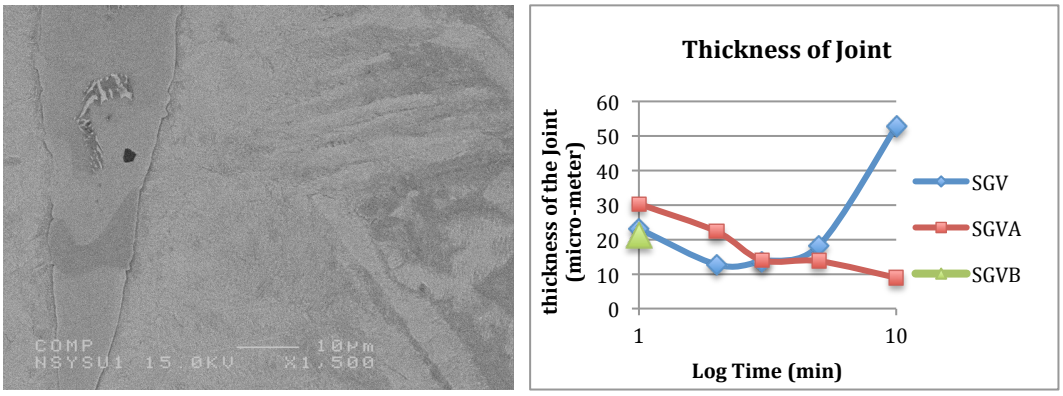

Figure 21 Cross-section of the joint by SEM-EPMA and microscope analysed the thickness variation of the joint with increasing time at different temperatures. The thickness of the joint region is calculated as average of 20 measurements each sample. S5GVA left (10 minutes). S4GVA, as shown in Fig 22 top (5 minutes.)

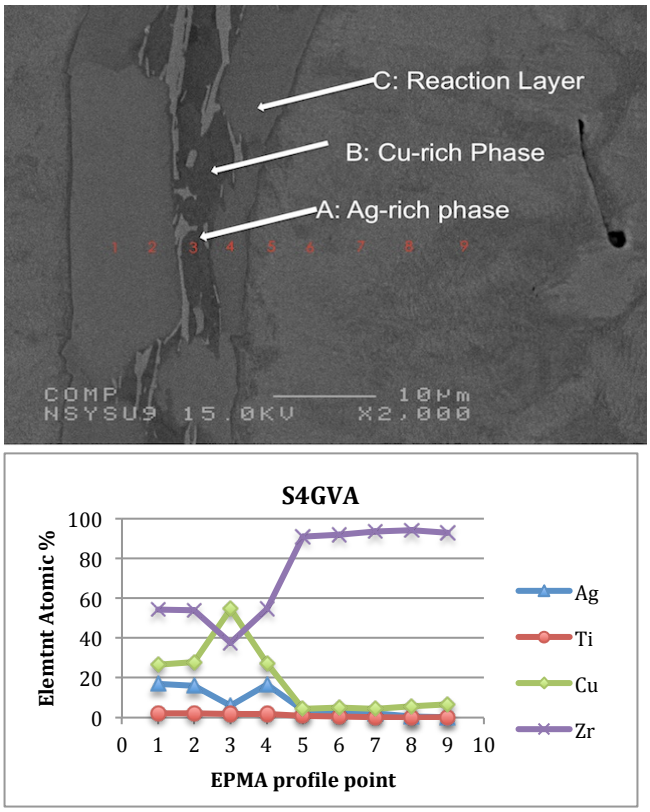

Figure 22 Composition profile and image of S4GVA. The trace marker (top) were measured from the braze alloy to the Zr substrate by SEM-EPMA. The plot below shows the composition profile of S4GVA and there is no oxide occurred while brazing in the vacuum system and under compression in the Gleeble.

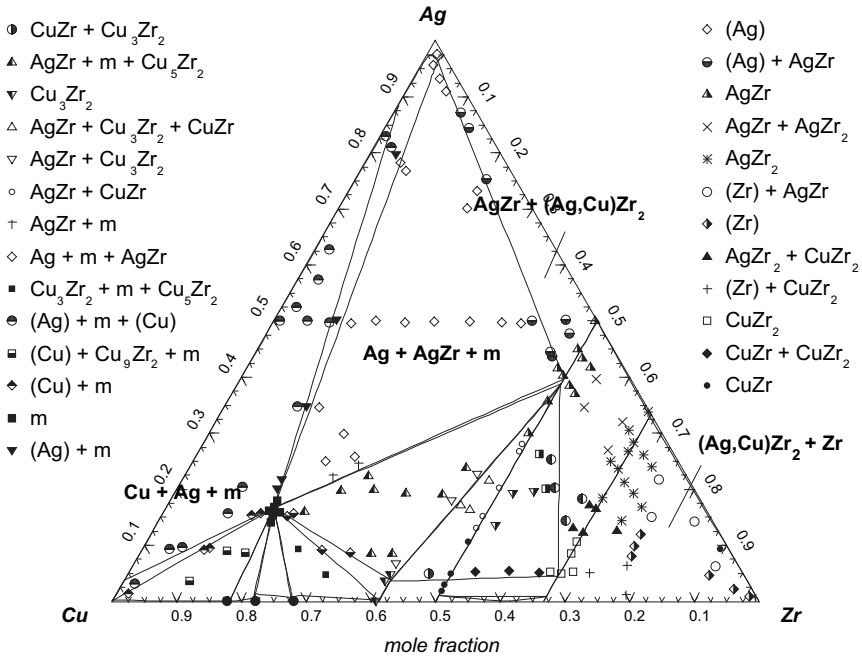

Figure 23 Schematic Zr-Cu-Ag ternary phase diagram illustrates the combination phases of each compositions. [82]

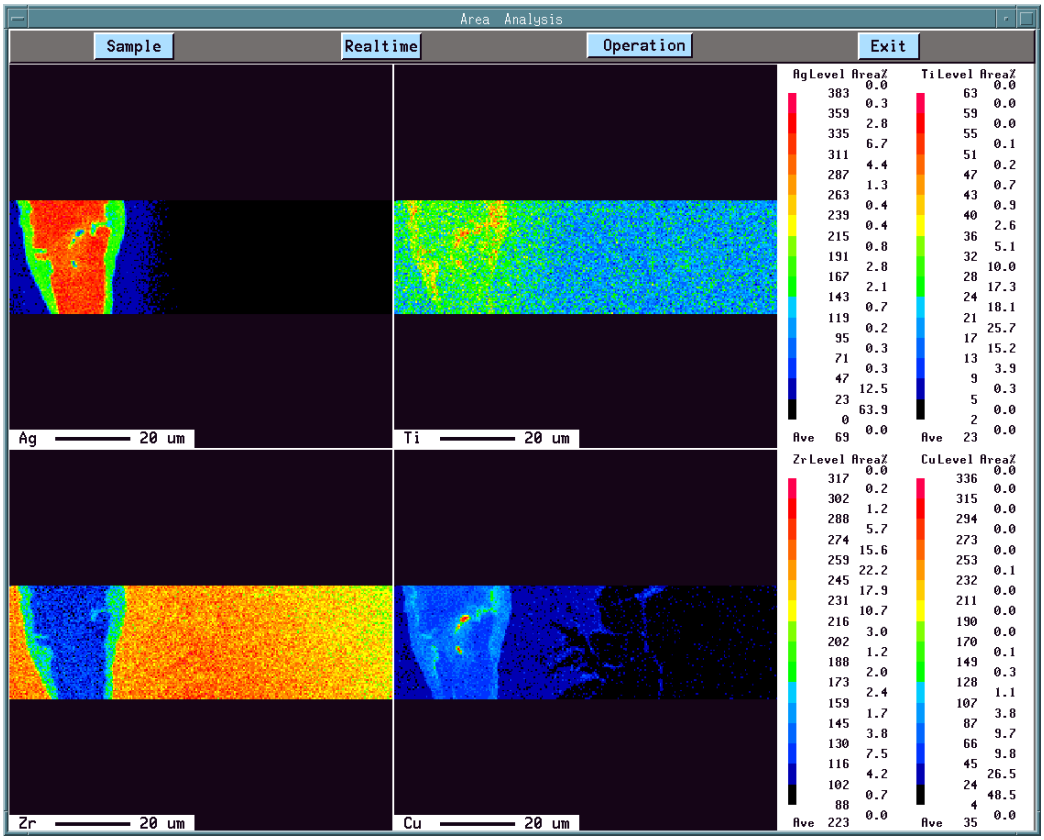

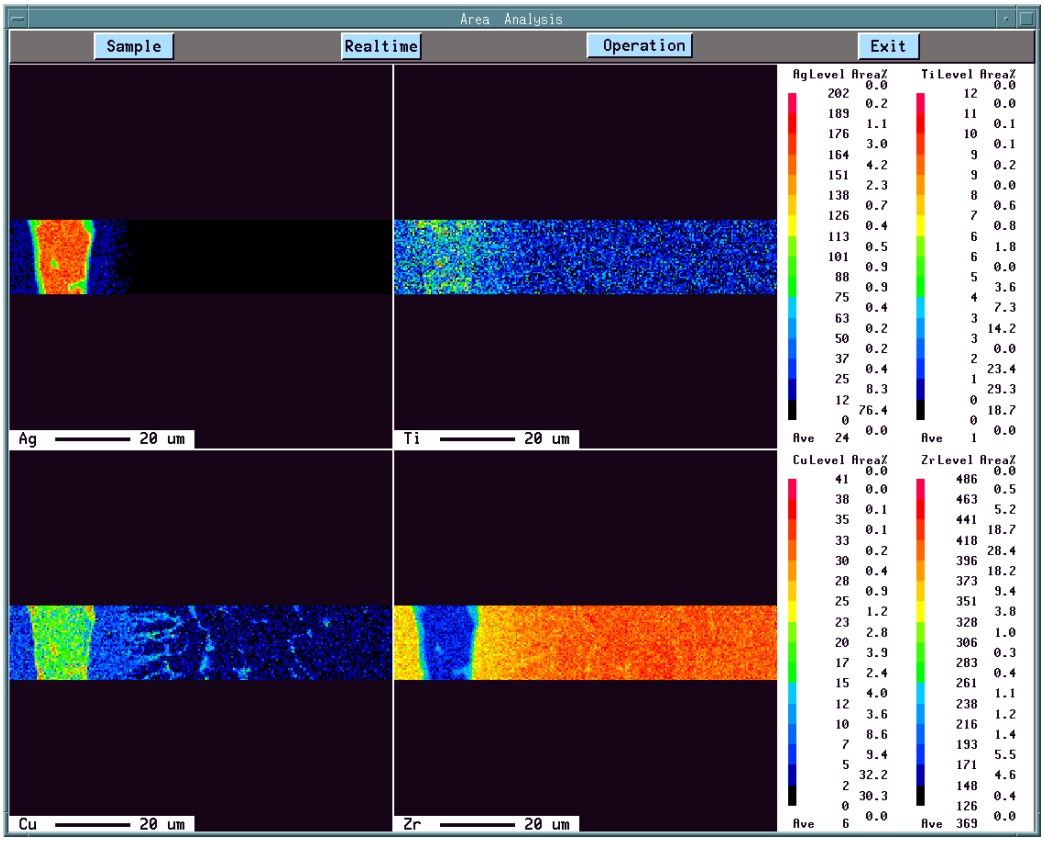

Figure 24 SGV Mapping by SEM-EPMA S1GV (top) and S2GV (bottom) at 940 °C

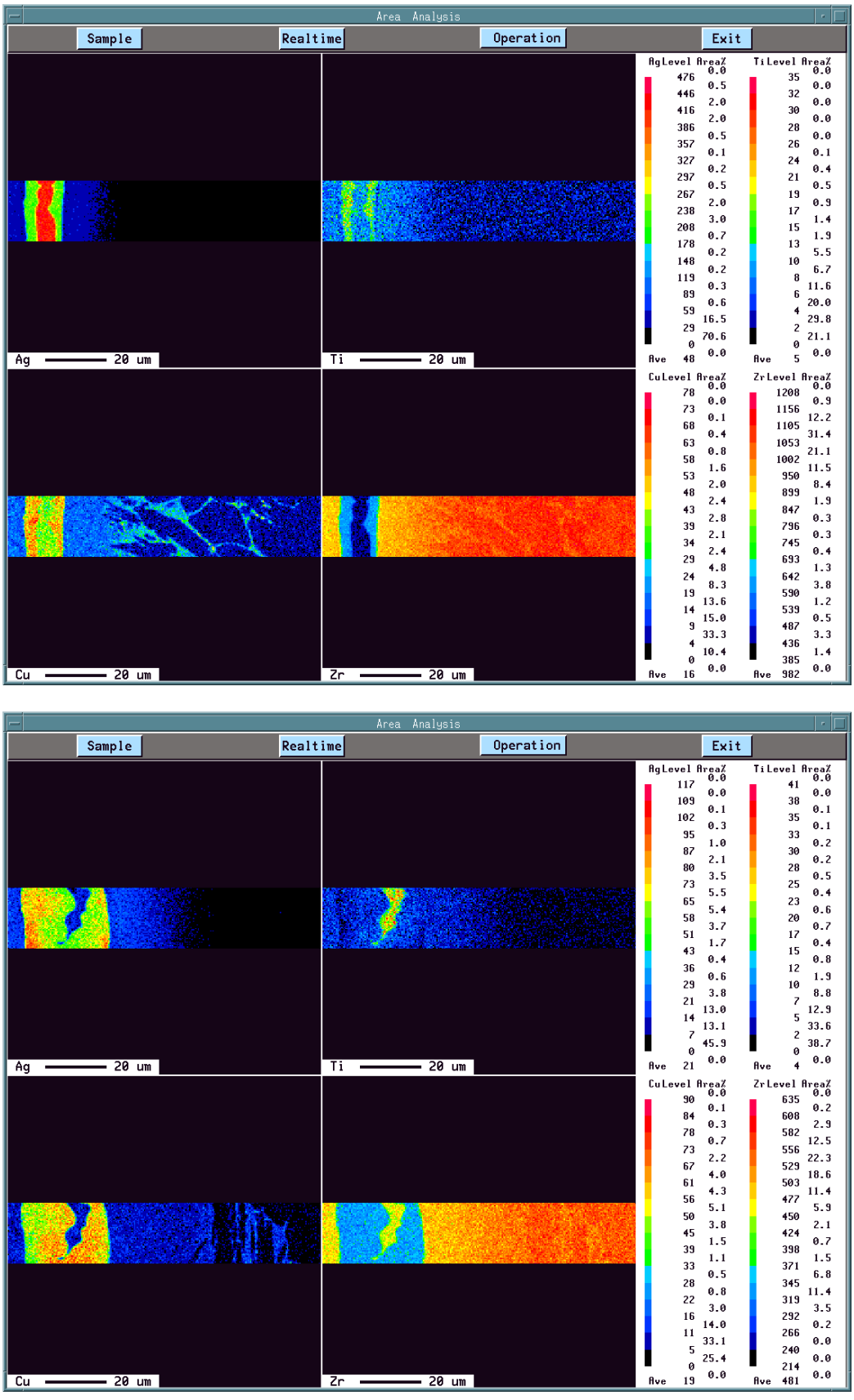

Figure 25 SGV Mapping by SEM-EPMA S3GV (top) and S4GV (bottom) at 940 °C

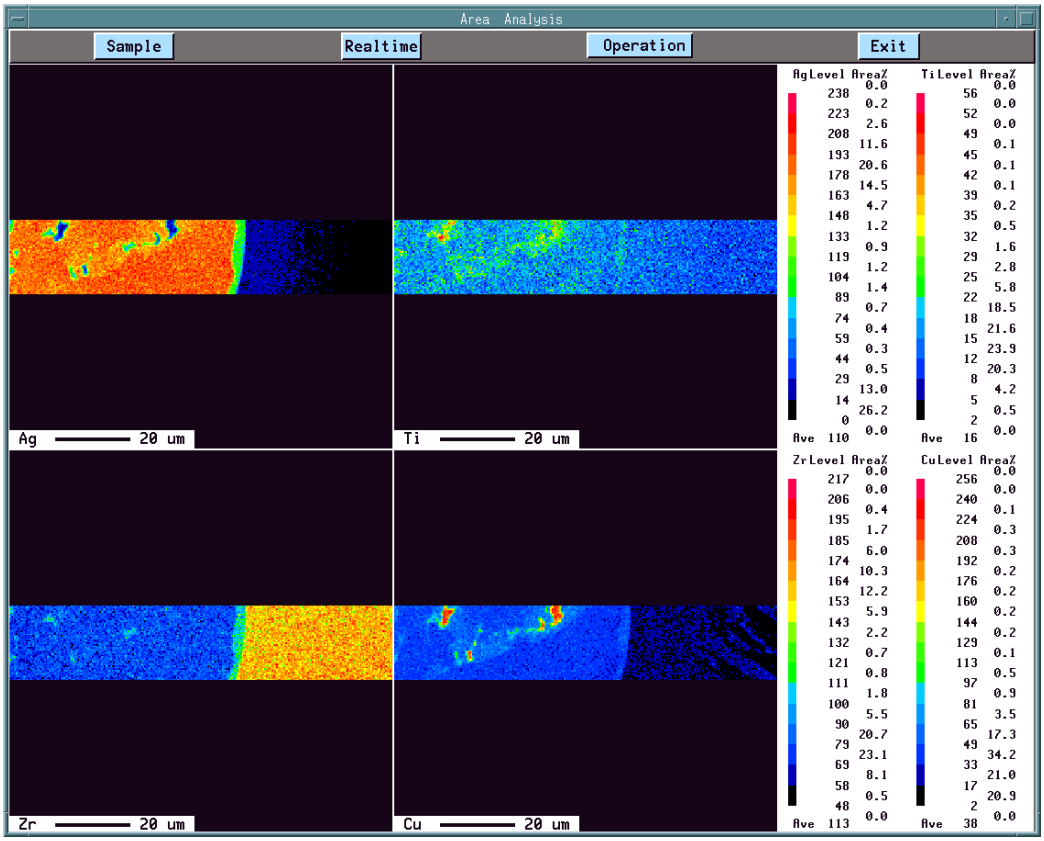

Figure 26 SGV Mapping by SEM-EPMA S5GV at 940 °C

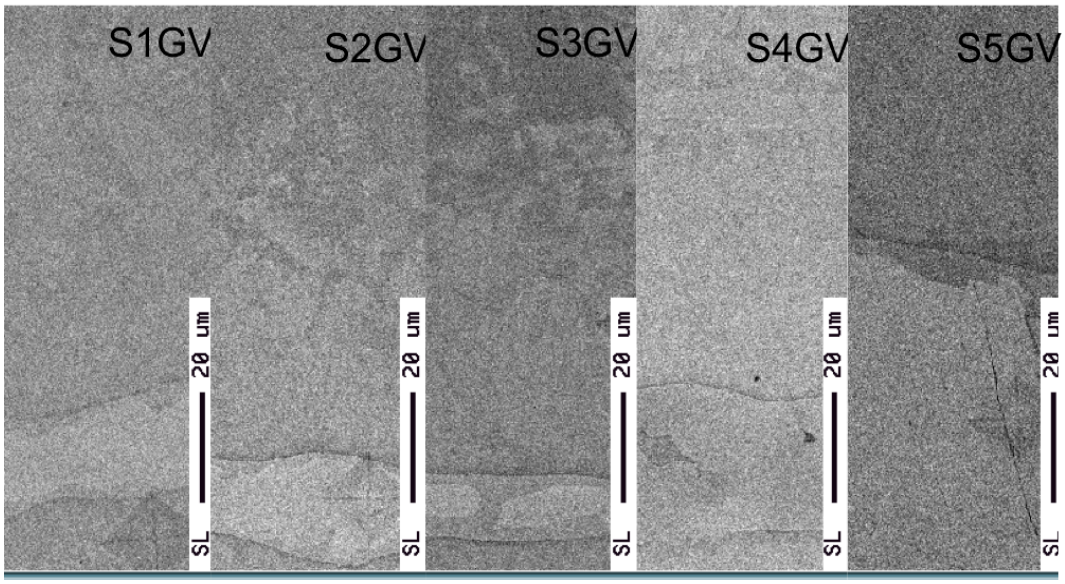

Figure 27 SEM microscopes of the joint and the substrate SGV series.

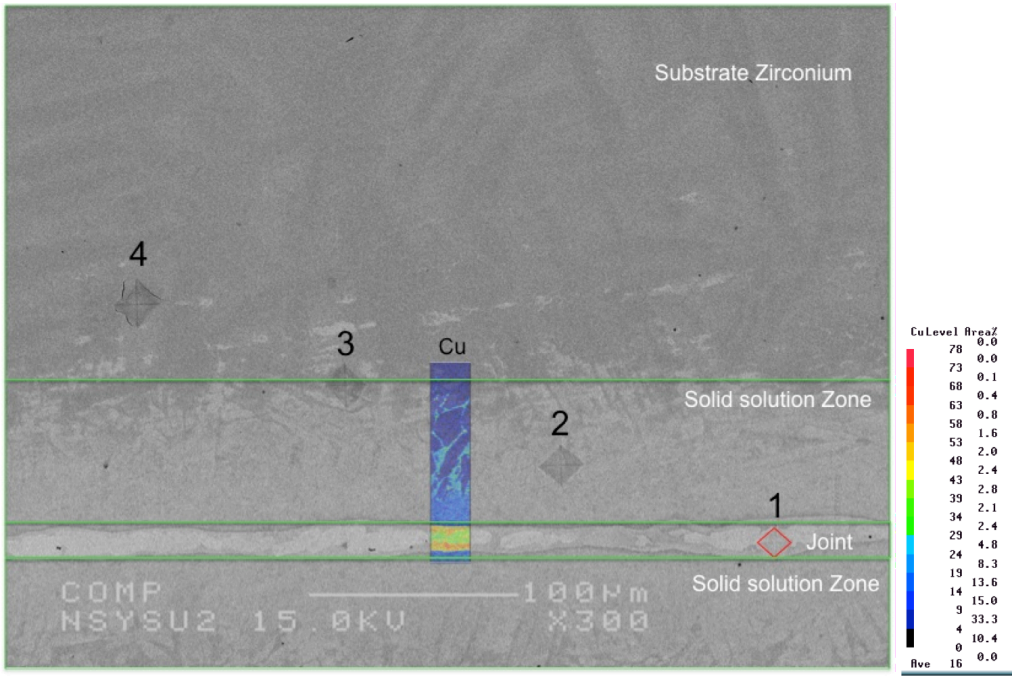

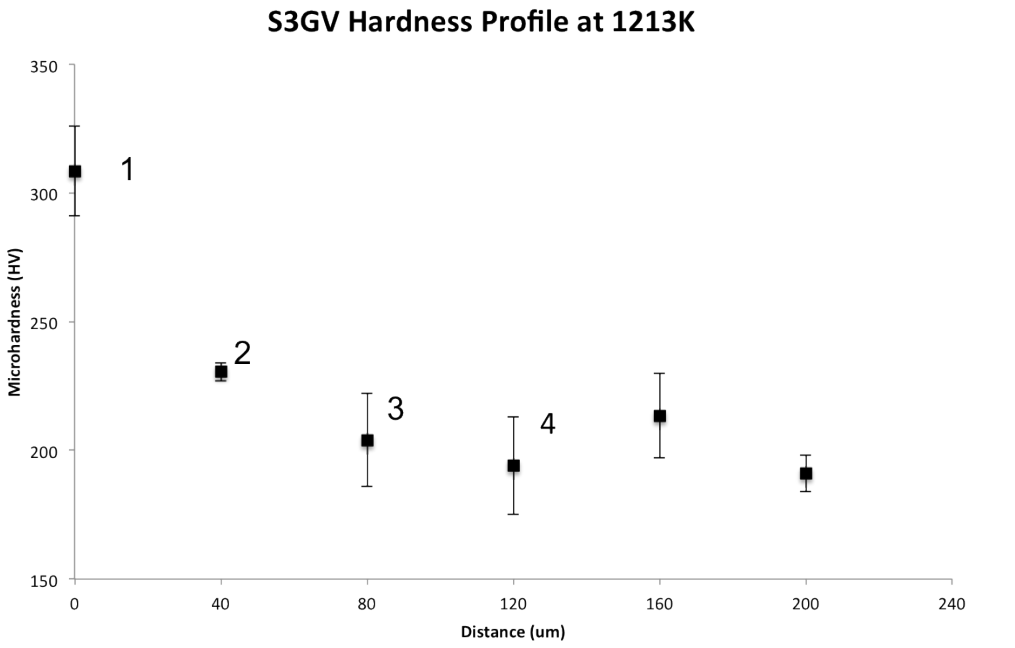

Figure 28 Microhardness is measured as above figure and the down plot is the profile image and data. The Cu quantity contained level was illustrated in the blue rectangle by SEM-EPMA mapping.

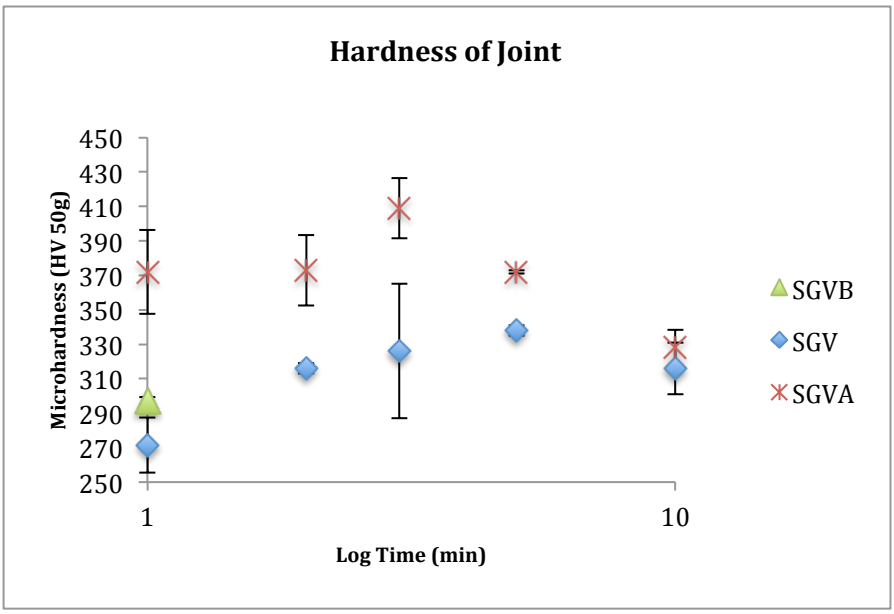

Figure 29 Microhardness of joint as a function of time at different brazing temperatures

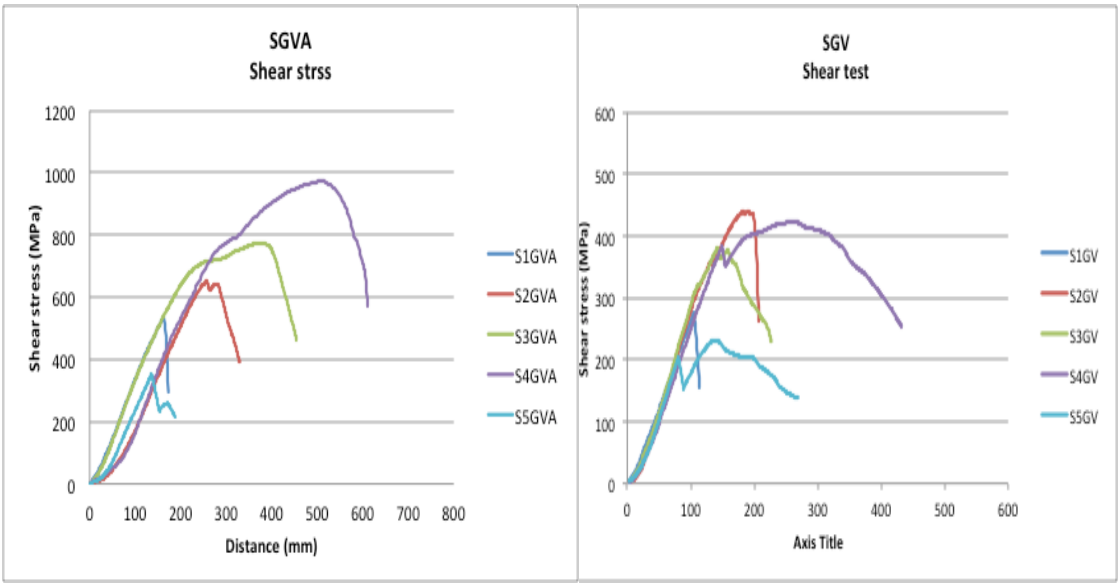

Figure 30 Shear strength value of brazed joints. SGVA (880 ^{o}C) shows higher value then SGV (940 ^{o}C) series of brazes. Brazing for 5 minutes (S4GV, S4GVA) resulted in higher strength at both temperatures.

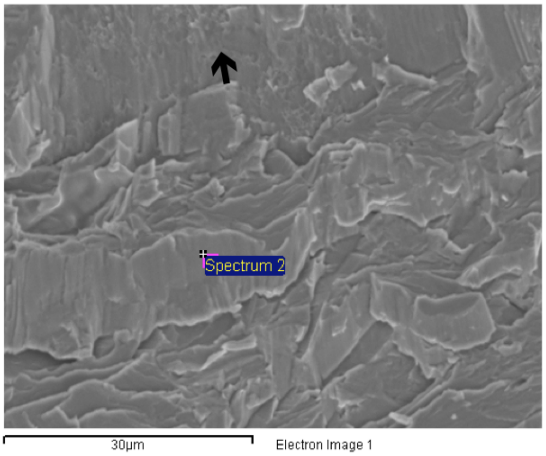

Figure 31 Image of S4GV fracture surface by SEM

Table 12 S4GV Fracture surface of element analysis by SEM-EDS.

Element	Atomic %
Zr	99.19
Cu	0.33
Ag	0.48
Ti	-

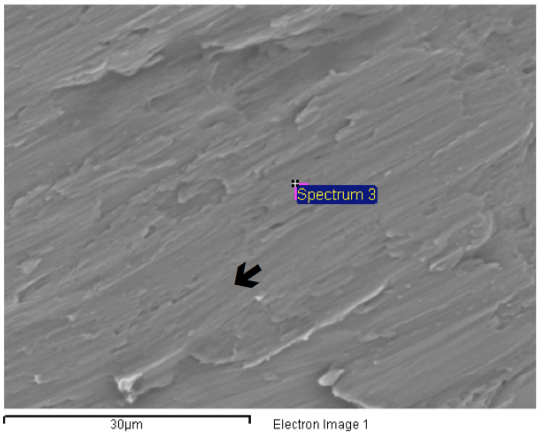

Figure 32 Image of S4GVA fracture surface by SEM

Table 13 S4GVA Fracture surface of element analysis by SEM-EDS

Element	Atomic %
Zr	82.09
Cu	9.97
Ag	7.35
Ti	0.60

6.5 Brazing Vitreloy 105 with Cusil ABA

6.5.1 Microstructure of Joint

Vitreloy 105 ($Zr_{52.5}Cu_{17.9}Ni_{14.6}Al_{10}Ti_5$) brazing with Cusil ABA ($Ag_{49.7}Cu_{47.2}Ti_{3.1}$ in at. %) was carried out at 780 °C (melting point of Cusil ABA) for 1 minute in the Gleeble under vacuum. The cross-section, shown in Figure 33, exhibited the brazed region (A) at about 20.8 µm thick. There is a reaction layer (B), which is about 3.1 µm thick between the filler and substrate on both sides. The results of EPMA mapping showed that the reaction layer is mainly formed of copper, silver, zirconium, nickel and small amounts of titanium and aluminium. Cu-Ag-Zr-Ti phase are mainly formed $Cu_{73.5}Ag_{14.45}Zr_9Ti_{2.7}$ as Cu-rich phases.

In the reaction layer, B, EPMA mapping, Figure 34, shows relatively uniform amounts of Ag and Cu present. Apart from Ti, all elements show a gradual decrease in concentration from braze to substrate or vice versa so that the composition in region B is generally between those for braze and substrate. This behaviour suggests that diffusion is occurring in one direction (either from braze to substrate or from substrate to braze) during brazing and post-braze cooling. In addition, Vitreloy 105 and Cusil ABA both contain large amounts of copper, which would encourage wettability and reaction for brazing. The behaviour of Ti would suggest limited solubility in the phase constituting region B, which may act as a partial diffusion barrier between braze and substrate. Moreover, the result of mapping (Figure 34) shows aluminium dissolved/diffused into the Ag-rich phase of the joint; the zirconium did not diffuse or dissolve appear in the reaction layer. This contrasts with the pure Zr brazing trials in this study, where zirconium either diffused into

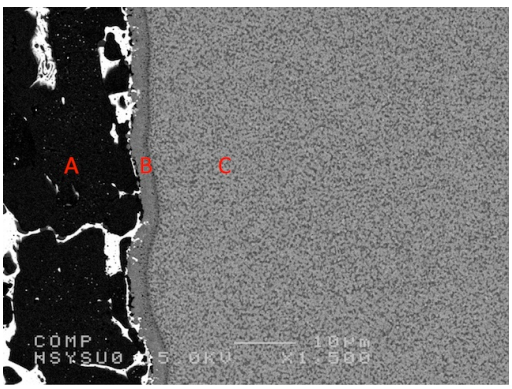

Figure 33 Cross-section of the joint, Vitreloy 105/Cusil ABA

the brazing alloy of Cu and Ag dissolved in solid zirconium, the reaction layer is formed of $Zr_{56.1}Ag_{19.6}Cu_{22.6}Ti_{1.7}$ (880 °C) and $Zr_{65.1}Ag_{19.4}Cu_{13.9}Ti_{1.6}$ (940 °C)

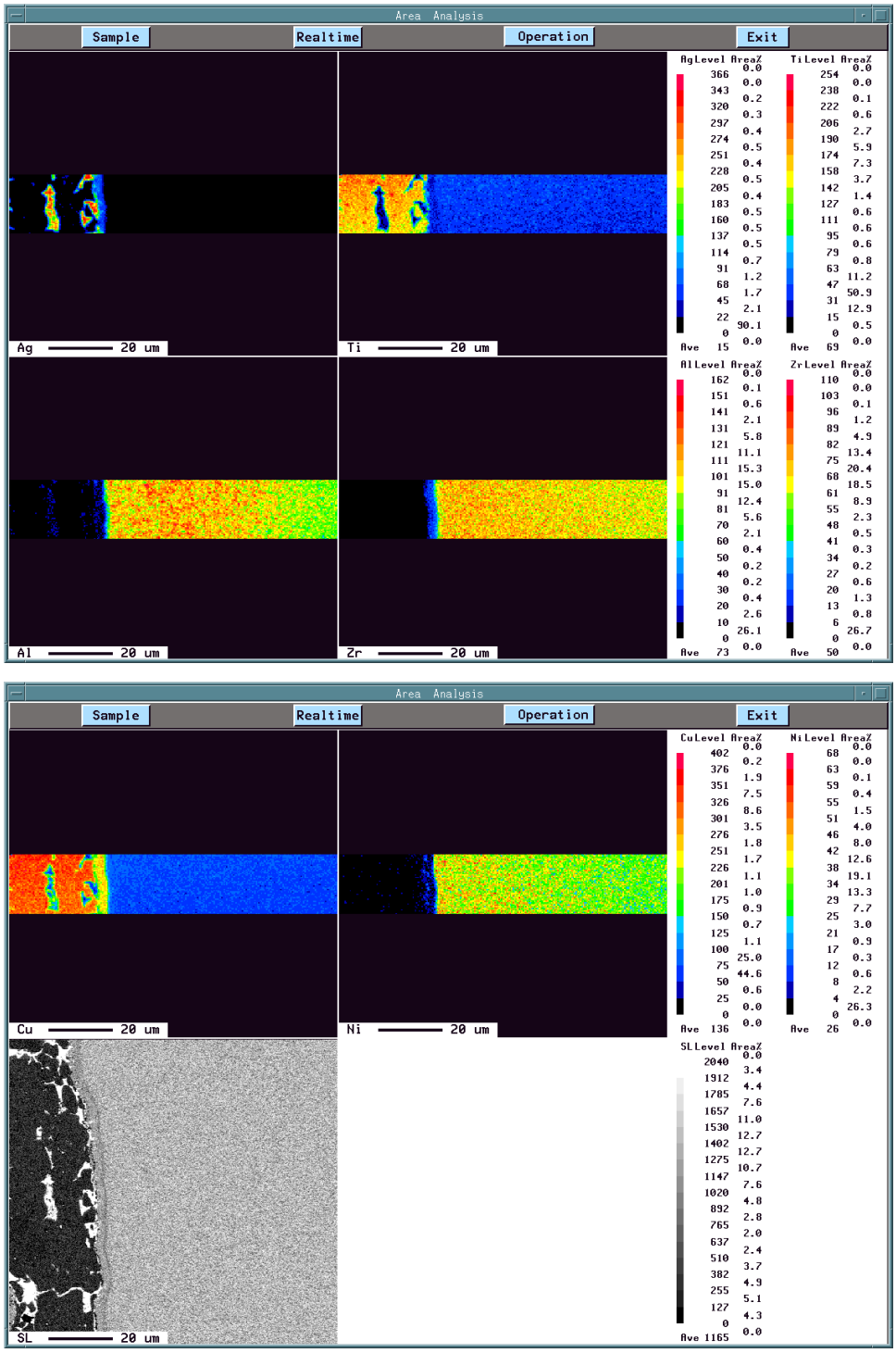

Figure 34 Mapping of the joint, Vitreloy 105/Cusil ABA by SEM-EPMA, to observe individual element diffusing between the braze alloy and Zr-based BMG at 780 °C. The left corner of bottom figure is the SEM image of joint cross-section

6.6 Discussion on Microstructure of Brazed Joints

From the experimental work in this study, the brazed joint was composed of two different parts. The reaction layer contained a very high amount of Cu that could be retained to form Cu-based amorphous material [82][93]. More importantly, the EPMA results show the reaction layer is based largely on the Zr-Ag-Cu system with potential effects on Vitreloy 105 properties discussed below.

The Zr-Cu-based amorphous system has been reported to vitrify over a wide range of compositions. Zr-based and Cu-based BMG alloys have not only high GFA, but also high strength and good mechanical properties. For the reaction layer, the amorphous Cu-Ag-Zr alloys have been studied to predict their amorphisation by Hoon et al. [82]. The possible behaviour of each composition has been calculated and shown in the amorphous formation diagram, Figure 34. Zhang et al. [94] reported the effect of higher content of Cu in Zr-based BMG, Vitreloy 1 ($Zr_{41.2}Ti_{13.8}Ni_{10}Be_{22.5}Cu_{12.5}$). Increasing of the content of Cu led the composition of Vitreloy 1, which is located near the eutectic point [95], farther from the eutectic point. Therefore, the GFA becomes worse. However, the result still shows that certain amounts of Cu (less than 23.7 at. % of Cu) can still maintain high GFA and also affect mechanical properties. The fracture strength increased by around 0.1 GPa, (from 2.1 GPa to 2.2 GPa), but the plasticity is reduced nearly zero when the content of Cu increased from 1.6-6 at. %. When the amount of Cu increased above 23.7 at. %, crystalline phases appeared in the amorphous matrix and the fracture strength reduced to only 1.8 GPa and giving completely brittle fracture.

6.6.1 The Effect of Additional Ag In Zr-Cu-Based Amorphous System

Certain amounts of Ag addition in the Zr-Cu based metallic glass can beneficially prevent the formation of intermetallic compounds. $(Cu_{0.618}Zr_{0.382})_{100-x}Ag_x$, $(Cu_{0.64}Zr_{0.36})_{100-x}Ag_x$, $(Cu_{0.5}Zr_{0.5})_{100-x}Ag_x$ and $Cu_{45}Zr_{45}Ag_xAl_{1-x}$ glassy alloys have been investigated [90-91] with compositions that are close to the Zr-Cu-Ag ternary eutectic. The combination of atomic size, shown in Figure 36 element radius, as one of the three Inoue empirical rules as discussed in Chapter 2.1 [21] that three or more dissimilar size of atoms (above about 12 % among the main constituent elements) accommodated in a unit cell will increase GFA for bulk metallic glasses. Moreover, the primary crystalline phase of $Zr_{65}Al_{7.5}Ni_{10}Cu_{12.5}Ag_5$ and $Zr_{65}Al_{7.5}Ni_{10}Cu_{7.5}Ag_{10}$ in metallic glasses has been reported to be an icosahedral phase [92-95]. Silver, Ag, is effective for the suppression of grain growth in $Zr_{65}Al_{7.5}Ni_{10}Cu_{7.5}Ag_{10}$, where the grain growth rate of icosahedral phase is about ten times less than the primary phase, Zr_2Ni phase, in $Zr_{65}Al_{7.5}Ni_{10}Cu_{17.5}$. The nucleation rate of the icosahedral phase, however, is reported approximately 10^4 times greater that that of the Zr_2Ni as shown in Table 14. The result shows the greater nucleation rate resulted from short-range ordering reflected by the strong chemical bond for Zr-Ag compared with Zr-Ni.

To summarise, evaluation of additional amounts of Cu and/or Ag in Vitreloy 105 could maintain its GFA and its good mechanical properties. However, composition of the reaction layer, $Cu_{73.5}Ag_{14.45}Zr_9Ti_{2.7}$, is farther away from the amorphous region in the prediction Zr-Cu-Ag diagram (Fig. 35), which would lead to crystallisation [82].

Table 14 The primary phase growth rates and nucleation rate by adding amount of Ag in Zr-based BMGs [92].

Alloy	Growth rate at T_x (ms^{-1})	Nucleation rate at T_x ($m^{-3}s^{-1}$)
$Zr_{65}Al_{7.5}Ni_{10}Cu_{17.5}$	$1.1x10^{-8}$	$2.6x10^{16}$
$Zr_{65}Al_{7.5}Ni_{10}Cu_{7.5}Ag_{10}$	$1.3x10^{-9}$	$3.8x10^{20}$

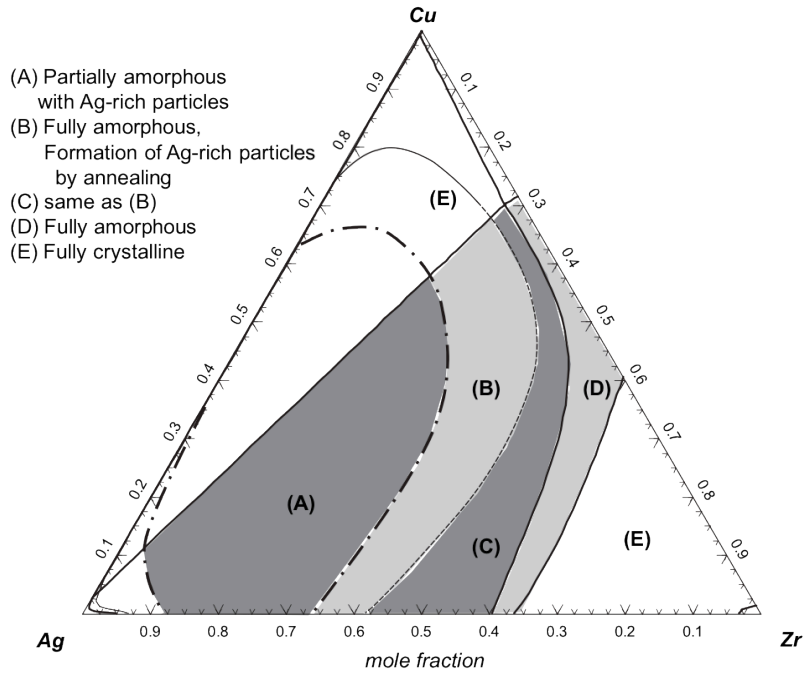

Figure 35 Ternary phase diagram of Cu-Zr-Ag illustrating the composition regions of possibilities of forming amorphous and crystalline behaviours. [82]

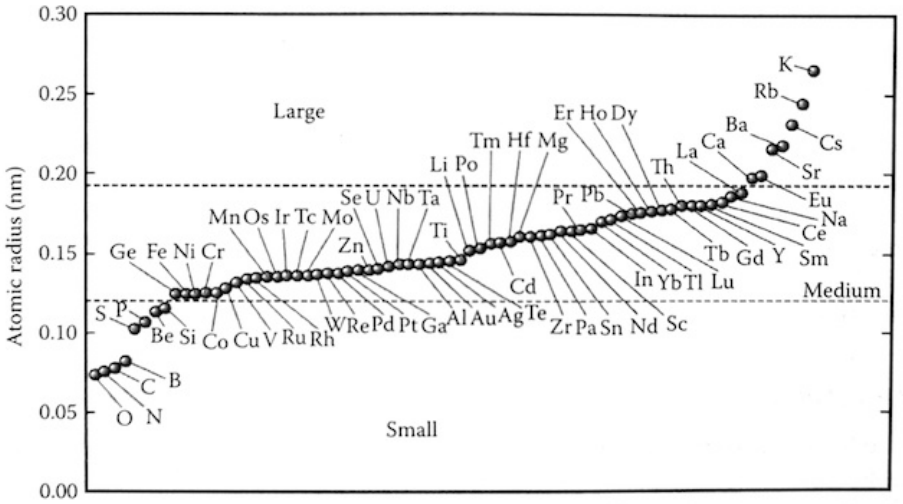

Figure 36 Schematic atomic radius for the elements. These have been divided into 3 main groups of atomic size, large, medium and small for forming BMGs. [11]

6.7 Mechanical Properties of Vitreloy 105 – Cusil ABA Brazed Joints

6.7.1 Microhardness.

The Vicker's microhardness of the Vitreloy 105 was recorded at about H_v: 680 in this study. After one minute of brazing with Cusil ABA, the profile is shown in Figure 37, the hardness of substrate is increased up to around H_v: 790 consistent with crystallisation effects. The joint hardness is similar to that recorded for Zr-Cusil ABA brazed joints at approximately H_v: 370.

6.7.2 Shear Strength

Shear testing of the Vitreloy 105 – Cusil ABA brazed joints showed an approximately linear loading line up to a brittle failure event, Figure 38. Failure occurred at a shear stress of 170 MPa, which is approximately an order of magnitude lower than the yield stress of Vitreloy 105. Despite the low hardness of the filler layer, failure occurred through the substrate. This indicates that the thermal exposure of the BMG resulted in embrittlement to such an extent that this was excessively notch-sensitive. Previous work [14] has shown that Vitreloy 105 remains ductile and hardens when the structure is nano-crystalline, but becomes brittle as the scale increases to micro. The brittle nature is shown by fractography, Figure 39, which exhibits brittle facets extending up to a 0.7 mm in size. The strong effect of such a short brazing cycle indicates that a braze with a melting temperature much closer (and ideally below) the crystalline temperature of the BMG (T_x = 473 ^{o}C) is needed.

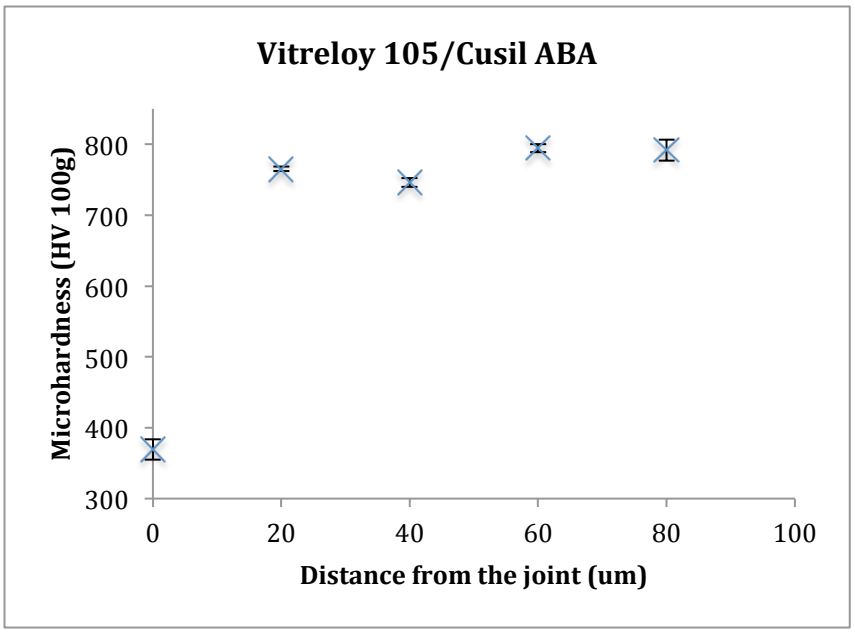

Figure 37 Microhardness (H_v: 100g) profile of Vitreloy 105/Cusil ABA joint at 780 °C. The original middle of the braze foil is at 0 mm and to the substrate either side.

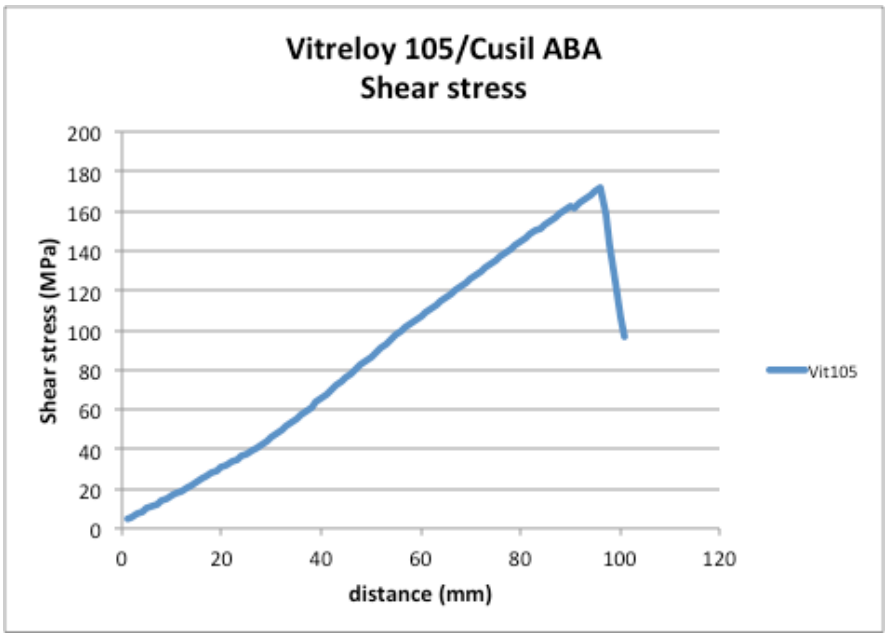

Figure 38 Shear stress of the joint, Vitreloy 105/Cusil ABA. Vitreloy 105 was sheared and become brittle after brazing at 780 °C resulting sheared the substrate, not the joint.

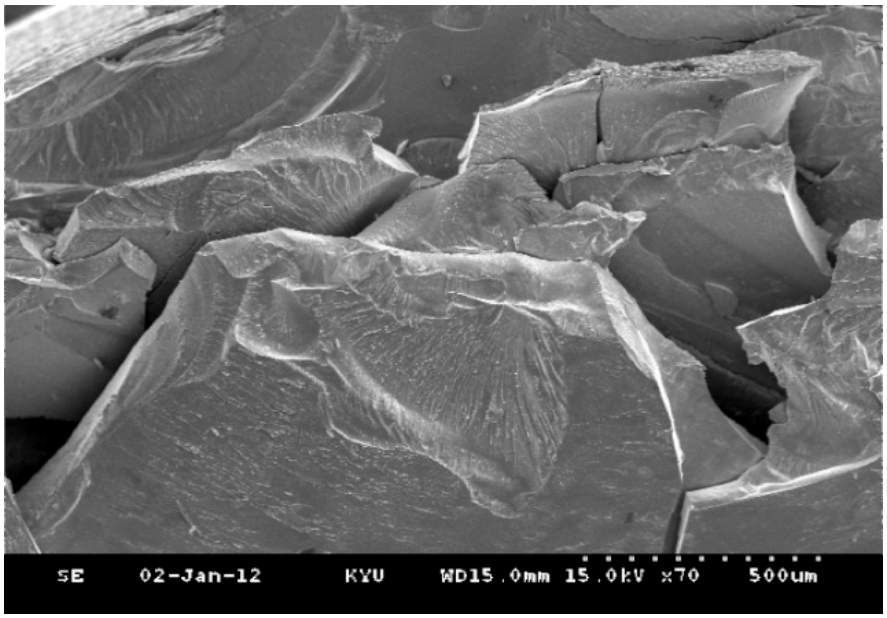

Figure 39 Fracture surface of the joint, Vitreloy 105/Cusil ABA. As the sharp edge and the shatter of glass form indicates that Vitreloy 105 was become brittle.

6.8 Conclusions

In this study, the brazing temperature was found to be excessively high for brazing of Zr-based alloys with Cusil ABA, especially for Vitreloy 105. However, this study gives insight into the fundamental mechanisms of brazing Zr and Zr-based BMGs. Both crystalline and amorphous Zr alloys reacted with Cu and Ag from the Cusil ABA braze foil. Vitreloy 105 (Zr-based BMG in this study) gave a reaction layer formed of Cu-Ag-Zr-Ti ($Cu_{73.5}Ag_{14.45}Zr_9Ti_{2.7}$) phase between the braze alloy and Vit105. Vitreloy 105 and braze alloy (Cusil ABA) both contain Cu, which would encourage wettability and reaction. Many studies [88-90][92-95] show that slightly higher copper and/or silver level could still be expected to form an amorphous phase and maintain the mechanical properties of Vitreloy 105. However, the reaction layer contains a high amount of Cu in the Cu-Zr-Ag system, which is a fully crystalline phase. This could be extended in further work to form Cu-based amorphous alloys or others BMGs in the joint by selecting lower content of Cu in the brazing alloy.

Brazing of the Zr-based BMG was not successful in this study as the Vitreloy 105 is exposed to temperatures above its crystallisation temperature (T_x) leading to a micro-crystalline structure or coarser, which exhibits excessively brittle behaviour. The objective of brazing Vitreloy 105 is to select the brazing temperature below the crystalline temperature within the supercooled liquid region (between glass transition temperature, T_g and T_x). In this study, a brazing alloy with similar mechanical properties to Vitreloy 105 would be needed for joining the face to the crown of a golf driver. Correspondingly, choosing brazing alloys with low melting point (below T_x) and high mechanical properties as high yield stress and low elastic modulus would be needed. Accordingly, Mg-based, Zn-based and Ca-based BMGs might be suitable for further work.

CHAPTER 7 FUTURE WORK

7.1 The Objective of Future Work

Little literature has been published on welding BMGs with themselves or other BMGs [41]. The purpose of further study is to determine which brazing alloys would give high yield strength, good wettability, ductility and joint strength for brazing with Vitreloy 105 ($Zr_{52.5}Cu_{17.9}Ni_{14.6}Al_{10}Ti_5$ BMG). More specifically, this braze will allow Vitreloy 105 (Vit105) and filler alloys to maintain their amorphous nature, which limits the brazing temperatures to between 420 and 435 ^{o}C (supercooled region below crystallisation temperature) [12]. A secondary purpose of this work will be to assess the accuracy of predictions based on Thermo-Calc software for reaction of amorphous alloys. If proven, this understanding of the behaviour between equilibrium and non-equilibrium alloys will aid alloy design.

7.2 Selection of Brazing Alloys.

Melting behaviour and mechanical properties have been used to select BMGs as potential brazes for Vitreloy 105 with high values of fracture strength. Liquidus temperatures (T_l) of the filler (brazing alloys) for BMG alloys are restricted by the crystallisation temperature (T_x = 440 ^{o}C) of the alloy substrate (Vit105) [12]. There are a range of potential alloys that have seen summarised in Table 15; these are either Mg-based [96-97], Zn-based [99], or Ca-based [100] BMG alloys. These alloys have been shown to have a good range of mechanical property values (for this application) whilst having a low melting point. A number of studies have shown that the Young's modulus values of Mg-based BMGs [11][97] are about 50 GPa; Ca-based BMGs [101] are about 20-30 GPa and Zn-based BMGs [99] also

have low Young's modulus values (there are very few reports that have been published about Zn-based BMGs)

Table 15 Properties of Mg-based, Zn-based and Ca-based bulk metallic glass. (Liquid temperature, T_l, Fracture strength σ_f thickness of BMGs D_c and Poisson's ratio (ν)

Alloy	T_l(K)	σ_f(MPa)	D_c(mm)	ν	Ref.
$Mg_{75}Cu_{14.5}Zn_{3.5}Y_7$	731	875 ± 30	3		[97]
$Mg_{61}Cu_{28}Gd_{11}$	737	1075 ± 35	12		[98]
$Mg_{65}Cu_{15}Ag_{10}Tb_{10}$	697	922-1035	6	0.32[20]	[96]
$Zn_{40}Mg_{11}Ca_{31}Yb_{18}$	667	663	-	-	[99]
$Ca_{65}Mg_{15}Zn_{20}$	640 ± 10	300-409	6	0.31[20]	[99] [100] [102]

Liquidus temperatures of the three braze alloys $Mg_{65}Cu_{15}Ag_{10}Tb_{10}$, $Zn_{40}Mg_{11}Ca_{31}Yb_{18}$ and $Ca_{65}Mg_{15}Zn_{20}$ BMGs are below the crystallisation temperature T_x = 440 ^oC of Vitreloy 105 substrate. Thermo-Calc has been used to predict the equilibrium reaction between substrate and braze prior to manufacture in order to estimate likely wettability and joint strength for future study.

7.3 Methods of Prediction

The prediction is based on the software program, Thermo-Calc, to calculate the amount and composition of stable phases as a function of composition, temperature and pressure as shown in the Experimental Methods Chapter 5. The melting range of each brazing alloy ($Mg_{65}Cu_{15}Ag_{10}Tb_{10}$, $Zn_{40}Mg_{11}Ca_{31}Yb_{18}$ and $Ca_{65}Mg_{15}Zn_{20}$ BMGs) was calculated on Version R of Thermo-Calc with SSOL2 database. Within these temperature ranges (Table 16) the stability of different mixes of braze and base material (from pure substrate to pure braze, e.g. 10% braze, 90% Vitreloy 105) was determined. This was used to determine the

composition range and end compositions for single and multiple phase regions from the braze metal into the substrate. The greater the composition range for a single phase structure then the greater the likely interdiffusion and so these parameters should relate to wettability and brazed joint strength.

Table 16 Melting range of three BMGs was calculated by the Thermo-Calc.

BMGs	Melting range (K)
$Mg_{65}Cu_{15}Ag_{10}Tb_{10}$	800~960
$Zn_{40}Mg_{11}Ca_{31}Yb_{18}$	803~882
$Ca_{65}Mg_{15}Zn_{20}$	923~978

7.4 Results and Discussion

The equilibrium phase fractions for each of the three selected brazes alloys reacting at their liquidus temperatures with Vitreloy 105 have been predicted using Thermo-Calc. The predictions have been carried out for different starting mixes of braze and substrate and so represent the equilibrium mix if the braze diffused into the substrate (without changing composition).

In the case of the Mg-based BMG braze, Figure 40(a), the effect of Mg on the stability of the solid Vitreloy 105 is very strong so that liquid persists down to 10% braze. This is in contrast with the Zn-based and Ca-based BMGs, where liquid is absent at brazes levels below 90%, Figures 41(a) and 42(a). The (predicted) ready penetration of liquid braze into Vitreloy 105 would suggest that chemical bonding would be easily established so that joint strength should be high. The ready reaction would suggest that wettability would also be high. The liquid phase is predicted to be lost to a eutectic mixture of AlNi and the hcp phase. The hcp phase should be Tb-rich, although Zr content increases with depth, but, as Zr is the matrix then growth would be controlled by diffusion of Tb and so would be slow allowing the

interaction volume to be controlled. Although the eutectic would not form, Thermo-Calc predictions give the driving forces for these changes and so indicate what diffusion profiles would be expected – essentially those shown in Figure 40(b). A secondary factor is copper, which was the highest mass fraction in the liquid braze composition. The presence of Cu in both braze and substrate would also tend to improve wettability as the present experiment shows that the reaction layer is formed of Cu-rich phases between Cusil ABA and Vitreloy 105.

Thermo-Calc predicts similar phase fraction and composition profiles for the Zn and Ca-based BMG / Vitreloy 105 combinations, Fig 41 and 42. As noted above, there is a rapid loss of liquid, which would reduce reaction and wettability compared with Mg-based BMG, but the presence of a semi-solid region does indicate that the combination is not non-wetting with the substrate. The semi-solid region represents solidification as an AlNi plus bcc eutectic and, as for the Mg-based BMG, would improve strength and wettability, but not to the same extent. Beyond the semi-solid region there is a gradual replacement of the bcc phase by AlNi at a shallow rate so that the driving force would be relatively stable. The solid-state transformation would require interdiffusion of Yb, Zn, Al and Ni for the Zn-based BMG (figure 41(b)) and so would be occur at a very slow rate; as for Tb, Yb is a lanthanide and so a very large atom. This suggests that the system will achieve a reasonable amount of wetting and joint strength through the limited semi-solid region before stopping, making it controllable.

The Ca-based BMG shows similar behaviour but the solid-state transformation now requires interdiffusion of Ca, Zn, Al and Ni (Fig 42(b)) and so would be more rapid suggesting that greater modification of the substrate may occur for the use of this BMG.

As a result, the Mg-based BMG would have the best wettability and joint strength then the Zn-based BMG and finally the Ca-based BMG based on these predictions. These predictions require experimental verification in the further study.

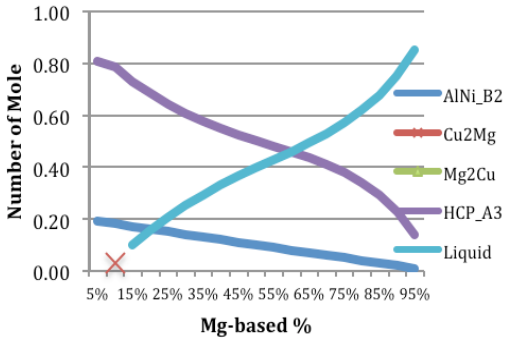

Figure 40(a) phase balance of mixtures of Mg-based BMG with Vitreloy 105 at 960 K

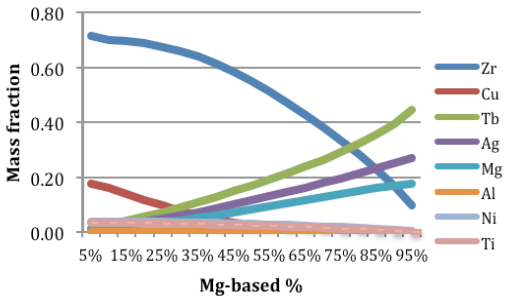

Figure 40(b) hcp phases composition of mixtures of Mg-based BMG with Vitreloy 105 at 960 K

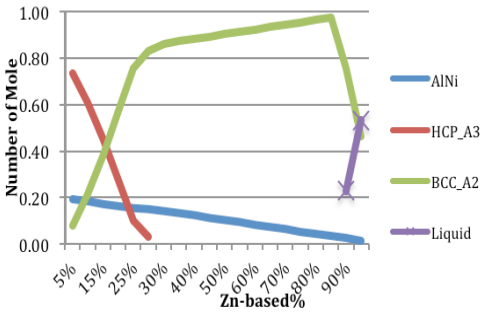

Figure 41(a) phases balance of mixtures of Zn-based BMG with Vitreloy 105 at 882 K

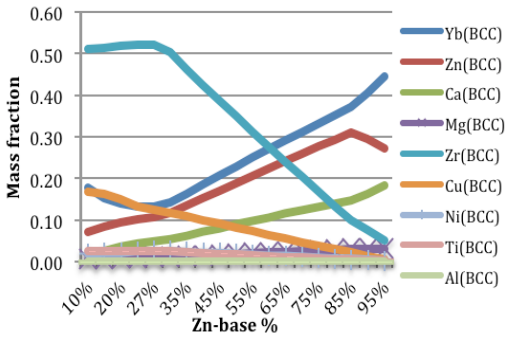

Figure 41(b) bcc phases composition of mixtures of Zn-based BMG with Vitreloy 105 at 882 K

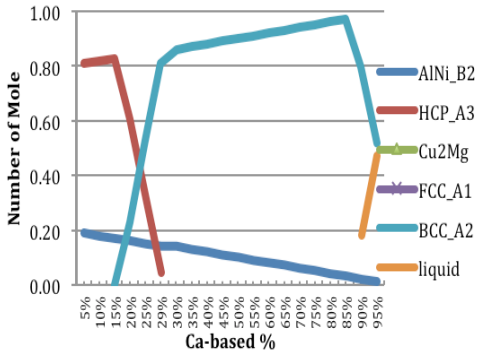

Figure 42(a) phases balance of mixtures of Ca-based BMG with Vitreloy1 105 at 978 K

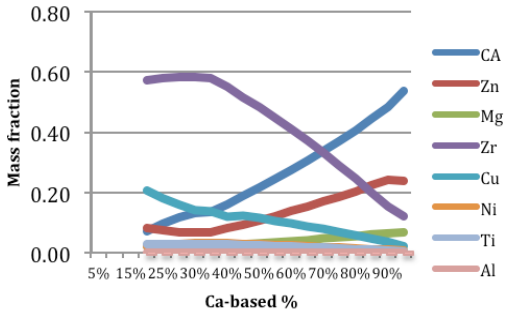

Figure 42(b) bcc phases composition of mixtures of Ca-based BMG with Vitreloy 105 at 978 K

7.5 Conclusions

In terms of mechanical properties, the Mg-based BMG has been reported to have a higher yield stress (~1.0 GPa) [11][96][103] and ductility [11][104] than the other two systems (Table 15). However, the cost of the Mg-based BMG is higher than the other two brazing alloys (Table 17). As shown in Table 15 and discussion of previous results, Zn-based BMGs have better strength, diffusion and wettability than Ca-based BMGs (Table 15). Although Ca-based BMGs have the lowest cost (Table 17), the properties from this report that they would form the least efficient joint.

Table 17 Cost of braze BMGs per unit mass

BMGs	Pound (£)/30g
$Mg_{65}Cu_{15}Ag_{10}Tb_{10}$	498.13
$Zn_{40}Mg_{11}Ca_{31}Yb_{18}$	148.42
$Ca_{65}Mg_{15}Zn_{20}$	58.1

Summary

The predictions made by Thermo-Calc need to first be verified due to the BMGs representing a non-equilibrium state. First, wettability of brazing alloys, the most important aspect of brazing, should be tested on Vitreloy 105. Understanding the interaction along with any interaction products of the molten brazing alloys placed on the matrix (Vitreloy 105). Secondly, microstructure and mechanical properties (joint strength) of joints will need to be determined by brazing cm-sized samples of two Vitreloy 105 using Mg-based, Zn-based and Ca-based BMG foils. Thirdly, investigation of the differences between the equilibrium (crystalline) and non-equilibrium (amorphous) behaviour of the alloys in terms of phase fractions, composition and diffusion profiles. This will allow the use of Thermo-Calc in designing brazing systems of this type to be verified. Based on the results of these studies the applicability of the three brazing alloys to use in high performance golf drivers will need to be discussed.

Reference:

1. Y. Kawamura, T.S., Y. Ohno *Welding technologies of bulk metallic glasses.* Journal of Non-Crystalline Solids, 2003. **317**: p. 152-157.
2. S. Adelman, S.R.O., and M. Strangwood, *Modelling vibration frequency and stiffness variations in welded Ti-based alloy golf driver heads*. Engineering of Sport 62006. pp. 323-328.
3. Strangwood, M., *Materials in Golf*. Materials in Sports Equipment, ed. M. Jenkins2003, Cambridge: Woodhead. pp129-159.
4. Shiue, R.H. and S.K. Wu, *Infrared brazing of Ti50Ni50 shape memory alloy using two Ag-Cu-Ti active braze alloys.* Intermetallics, 2006. **14**(6): p. 630-638.
5. Hanson, W.B., K.I. Ironside, and J.A. Fernie, *Active metal brazing of zirconia.* Acta Materialia, 2000. **48**(18-19): p. 4673-4676.
6. Sciti, D., A. Bellosi, and L. Esposito, *Bonding of zirconia to super alloy with the active brazing technique.* Journal of the European Ceramic Society, 2001. **21**(1): p. 45-52.
7. Cochran, A.J.a.S., J, *Search for the Perfect Swing* 1968, Chicago: Triumph Books.
8. C. Suryanarayana, A.I., *Bulk Metallic Glasses* 2010: Taylor and Francis Group, LLC.
9. Widmann, H., *Characterisation of crystallisation kinetics and mechanical properties of an amorphous Zr-based metallic glass*, in *Metallurgy and Materials* 2008, University of Birmingham: Birmingham.
10. USGA, *Procedure for measuring Velocity Ratio of a Club Head for Conformance to Rule 4-1e* 1999, Far Hills, NJ: USGA.
11. Faulkner, E., *Characterisation and modelling of oversized golf drivers during impact phenomena.*, 2004, University of Birmingham: Birmingham.
12. Peker, A.a.W.L.J., *A highly processable metallic glass: Zr41.2 Ti13.8 Cu12.5 Ni10 Be22.5.* Applied Physics Letters, 1993 **63:17**: p. 2342-2344.
13. G. He, Z.B., And G.L. Chen, , *Structures and properties of a Zr-based bulk glass alloy after annealing* Materials Science and Engineering A, 1999. **270**: p. 291.
14. C. T. Liu, L.H., D. S. Easton, C. A. Carmichael, J. H. Schneibel, C. H. Chen, J. L. Wright, M. H. Yoo, J. A. Horton, and A. Inoue, *Test Environments and Mechanical Properties of Zr-based Bulk Amorphous Alloys.* Metallurgical and Materials Transactions A, 1998. **29A**: p. 1811-1820.
15. J. G. Wang, B.W.C., T. G. Nieh, and C. T. Liu, *Crystallization and nanoindentation behaviour of a bulk Zr-Al-Ti-Cu-Ni amorphous alloy.* Journal of Materials Research, 2000. **15**: p. 798-807.
16. Dauskardt, K.M.F.a.R.H., *Enhanced toughness due to stable crack tip damage zones in bulk metallic glass.* Scripta Materialia, 1999. **41**: p. 937.
17. C. J. Gillbert, V.S., and R. O. Ritchie, *Mechanisms for Fracture and Fatigue-Crack Propagation in a Bulk Metallic Glass.* Metallurgical and Materials Transactions A, 1999. **30A**: p. 1739-1754.
18. Lewandowski, P.L.a.J.J., *Fracture toughness and notched toughness of bulk amorphous alloy: Zr-Ti-Ni-Cu-Be.* Scripta Materialia, 1998. **38**: p. 1811.
19. Raghavan, R., Shastry, V. V., Kumar, A, Jayakumar, T., Ramamurty, U.,, *Toughness of as-cast and partially crystallized composites of a bulk metallic glass.* Intermetallics, 2009. **17**(10): p. 835-839.

20. Lu, Z.P., Y. Liu, and C.T. Liu, *Evaluation Of Glass-Forming Ability*, in *Bulk Metallic Glasses*, M. Miller and P. Liaw, Editors. 2008, Springer US. p. 87-115.
21. Inoue, A., *Recent Progress of Zr-Based Bulk Amorphous Alloys.* Science reports of the Research Institutes, Tohoku University. Ser. A, Physics, chemistry and metallurgy, 1996. **42**(1): p. 1-11
22. Akihisa, I., *Stabilization of Supercooled Liquid and Opening-up of Bulk Glassy Alloys.* Proceedings of the Japan Academy. Ser. B: Physical and Biological Sciences, 1997. **73**(2): p. 19-24
23. Inoue, A., *Bulk amorphous alloys: preparation and fundamental characteristics*1998, Uetikon-Zurich, Switzerland: Trans Tech Publications.
24. Turnbull, D., *Under what conditions can a glass be formed?* Contemporary Physics, 1969. **10**(5): p. 473-488.
25. Akihisa Inoue, T.Z.a.T.M., *Zr-Al-Ni amorphous alloys with high glass transition temperature and significant supercooled liquid region.* JIM, 1990. **31**: p. 177-183.
26. Ahmadzadeh, M. and B. Cantor, *Interstitial structure and diffusion in DRP metallic glasses.* Journal of Non-Crystalline Solids, 1981. **43**(2): p. 189-219.
27. F.E. Luborsky, *Ferromagnetic Materials*, ed. E.P. Wohlfahrt. Vol. 1. 1980, Amsterdam: North Holland.
28. G.M, H., *Point defect diffusion in alpha-Zr.* Journal of Nuclear Materials, 1988. **159**(0): p. 149-175.
29. Lu ZP, L.Y., Ng SC, *Reduced glass transition temperature and glass forming ability of bulk glass forming alloys.* J. non-cryst. solids, 2000. **270**: p. 103-114.
30. Z.P. Lu, H.T., Y. Li and S.C. Ng, *The correlation between reduced glass transition and the glass forming ability of bulk metallic glasses.* Scripta Materialia, 2000. **42**: p. 667-673.
31. Theodore A. Waniuk, J.S., and William L. Johnson, *Critical Cooling rate and thermal stability of Zr-Ti-Cu-Ni-Be alloys.* Applied Physics Letters, 2000. **78**(9): p. 1213.
32. L. Q. Xing, P.O., M. Harmelin, F. Faudot, and J. Bigot, *Alloys of high glass-forming ability.* Journal of Non-Crystalline Solids, 1996. **205-207**: p. 597.
33.. Inoue, A., Zhang, W., Zhang, T., Kurosaka, K., *High-strength Cu-based bulk glassy alloys in Cu-Zr-Ti and Cu-Hf-Ti ternary systems.* Acta Materialia, 2001. **49**(14): p. 2645-2652.
34. Tao Zhang, K.K.a.A.I., *Thermal and Mechanical Properties of Cu-based Cu-Zr-Ti-Y Bulk Glassy Alloys.* The Japan Institute of Metals, 2001. **42**(10): p. 2042-2045.
35. Zhang, T. and A. Inoue, *Ti-based amorphous alloys with a large supercooled liquid region.* Materials Science and Engineering: A, 2001. **304,Äì306**(0): p. 771-774.
36. Long, Z., et al., *A new criterion for predicting the glass-forming ability of bulk metallic glasses.* Journal of Alloys and Compounds, 2009. **475**(1-2): p. 207-219.
37. Elliott, R., *Eutectic solidification processing, crystalline and glassy alloys*1983: Butterworth-Heinemann Ltd.
38. Tanner, L.E. and R. Ray, *Metallic glass formation and properties in Zr and Ti alloyed with Be-I the binary Zr-Be and Ti-Be systems.* Acta Metallurgica, 1979. **27**(11): p. 1727-1747.
39. Turnbull, D., *Amorphous solid formation and interstitial solution behavior in metallic alloy systems.* J. Phys. Colloq., 1974. **35**: p. C4-1-C4-10.
40. Kawamura, Y., *Liquid phase and supercooled liquid phase welding of bulk metallic glasses.* Materials Science and Engineering: A, 2004. **375-377**(0): p. 112-119.

41. Hyung-Seop Shin, Y.-J.J., Ho-Yeon Choi, Hidemi Kato, Akihisa Inoue, *Joining of Zr-based bulk metallic glasses using the friction welding method.* Journal of Alloys and Compounds, 2007. **434-435**(0): p. 102-105.
42. Kawamura, Y., T. Shoji, and Y. Ohno, *Welding technologies of bulk metallic glasses.* Journal of Non-Crystalline Solids, 2003. **317**(1-2): p. 152-157.
43. Wang, H.-S., Chiou, M.-S., Chen, H.-G., Jang, Jason Shian-Ching., *The effects of initial welding temperature and welding parameters on the crystallization behaviors of laser spot welded Zr-based bulk metallic glass.* Materials Chemistry and Physics, 2011. **129**(1-2): p. 547-552.
44.. Kuo, P.-H., Wang, S.-H., Liaw, Peter K., Fan, G.-J., Tsang, H.-T., Qiao, D., Jiang, F., *Bulk-metallic glasses joining in a supercooled-liquid region.* Materials Chemistry and Physics, 2010. **120**(2-3): p. 532-536.
45. Mel M. Schwartz, S.A., *Fundamentals of Brazing*. ASM Handbook, Welding, Brazing, and soldering. Vol. 6. 1993: ASM International
46. S.D. Brandi, S.L., J.E. Indacochea and R. Xu, *Brazeability and solderability of Engineering Materials*. ASM Handbook, Welding, Brazing and Soldering. Vol. 6. 1993: ASM International
47. Bondi, A., *Spreading of Liquid Metals on Solid surface Chemistry of High Energy Substances.* Chem. Rev., 1953. **52 No.2**: p. 417-458.
48. Peter Atkins, J.d.P., *The temperature dependence of reaction rates*, in *Physical Chemistry*2002, Oxford University Press: Oxford. p. 879-881.
49. D. A. Porter and K. E. Easterling, *Phase Transformations in Metals and Alloys*. 2 ed, ed. T.F. Group1992: CRC Press.
50. Crank, J., *The mathematics of diffusion*1979: Clarendon Press.
51. M. Kijek, M.A., B. Cantor and R.W. Cahn, *Diffusion in Amorphous Alloys.* Scripta Metallurgica, 1980. **14**: p. 1337-1340.
52. M. Ahmadzadeh, B.C., J. non-cryst. . **Sol., in press**.
53. Faupel, F., et al., *Diffusion in metallic glasses and supercooled melts.* Reviews of Modern Physics, 2003. **75**(1): p. 237-280.
54. R.W. Cahn, J.E.E., J. Patterson, R.E. Somekh, & C.Kenway Jackson, Materials Science, 1980. **15**: p. 702.
55. Lesueur, C.B.D., Physic Stat.Sol., 1976. **A36**: p. 247.
56. Frank, W., Horner, A, Scharwaechter, P., Kronmuller, H., *Diffusion in amorphous metallic alloys.* Materials Science and Engineering: A, 1994. **179-180, Part 1**(0): p. 36-40.
57. Zhu, A., G.J. Shiflet, and S.J. Poon, *Diffusion in metallic glasses: Analysis from the atomic bond defect perspective.* Acta Materialia, 2008. **56**(14): p. 3550-3557.
58. Bartsch, A., Zöllmer, V., Rätzke, K., Meyer, A., Faupel, F., *Diffusion and viscous flow in bulk glass forming alloys.* Journal of Alloys and Compounds, 2011. **509, Supplement 1**(0): p. S2-S7.
59. Tamura, S., Tsunekawa, Y., Okumiya, M. Hatakeyama, M., *Ultrasonic cavitation treatment for soldering on Zr-based bulk metallic glass.* Journal of Materials Processing Technology, 2008. **206**(1-3): p. 322-327.
60. Nishikawa, H., WongPiromsarn, K., Abe, H., Takemoto, T., Fukuhara, M., Inoue, A., *Solderability of Bulk Metallic Glasses Using Lead-Free Solders.* MATERIALS TRANSACTIONS, 2009. **50**(6): p. 1326-1329.

61. Shin, H.-S., J.-S. Park, and Y. Yokoyama, *Dissimilar friction welding of tubular Zr-based bulk metallic glasses.* Journal of Alloys and Compounds, 2010. **504, Supplement 1**(0): p. S275-S278.
62. International, A., *Alloy Phase Diagrams*. ASM Handbook. Vol. 3. 1992, The Materials Information Company: ASM International.
63. Anderko, D.P.M.H.a.D.R.n.K., *Constitution of Binary Alloys* 2ed. Metallurgy and metallurgical Engineering Series, ed. R.F.M.a.M.B. Bever1958: McGraw-Hill Book company
64. C.J, R., *Oxidation of zirconium - A critical review of literature.* Journal of the Less Common Metals, 1968. **16**(3): p. 173-201.
65. V. N. Konev, A.L.N., and L. A. Minyacheva, *Mechanism of Oxygen Dissolution in Metallic Zirconium.* Oxidation of Metals, 1997. **74**(Nos. 3/4): p. 237-245.
66. Ritchie, I.G. and A. Atrens, *The diffusion of oxygen in alpha-zirconium.* Journal of Nuclear Materials, 1977. **67**(3): p. 254-264.
67. Madeyski, A., D.J. Poulton, and W.W. Smeltzer, *Parabolic oxidation kinetics of alpha-zirconium.* Acta Metallurgica, 1969. **17**(5): p. 579-584.
68. Garcia, E.A. and J. Kovacs, *Diffusion model for the oxidation of zirconium at 573 and 623 K.* Journal of Nuclear Materials, 1994. **210**: p. 78-83.
69. Rosa, C.J. and W.W. Smeltzer, *The parabolic oxidation kinetics of beta-zirconium.* Acta Metallurgica, 1965. **13**(2): p. 55-60.
70. Kofstad, Ö.a., *Oxidation of Zirconium and Zirconium-Oxygen Alloys at 8oo degree C.* Journal of The Electrochemical Society, 1962. **109**(3): p. 204-207.
71. Tanabe, T. and M. Tomita, *Surface oxidation of zirconium above room temperature.* Surface Science, 1989. **222**(1): p. 84-94.
72. Debuigne, J. and P. Lehr, *STUDY OF THE OXIDATION OF NON-ALLOYED ZIRCONIUM AND OF OXYGEN DIFFUSION IN THE OXIDE FILM AND IN THE METAL.* Journal Name: Mem. Sci. Rev. Met.; Journal Volume: Vol: 60; Other Information: Orig. Receipt Date: 31-DEC-64, 1963: p. Medium: X; Size: Pages: 911-23.
73. Douglass, D.L., *CORROSION MECHANISM OF ZIRCONIUM AND ITS ALLOYS--DIFFUSION OF OXYGEN IN ZIRCONIUM DIOXIDE*, in *Other Information: Orig. Receipt Date: 31-DEC-63*1962. p. Medium: X; Size: Pages: v.
74. Smith, T., *Diffusion Coefficients and Anion Vacancy Concentrations for the Zirconium-Zirconium Dioxide System.* Journal of The Electrochemical Society, 1965. **112**(6): p. 560-567.
75. Rosa, C.J. and W.C. Hagel, *Oxygen-ion diffusivity in hypostoichiometric zirconium dioxide.* Journal of Nuclear Materials, 1968. **27**(1): p. 12-20.
76. Hsieh, H.H. Kai, W., Huang, R. T., Pan, M. X., Nieh, T. G., *Effect of Zr-content on the oxidation and phase transformation of Zr-base amorphous alloys in air.* Intermetallics, 2004. **12**(10-11): p. 1089-1096.
77. Kim, C.W., H.G. Jeong, and D.B. Lee, *Oxidation of Zr65Al10Ni10Cu15 bulk metallic glass.* Materials Letters, 2008. **62**(4-5): p. 584-586.
78. Mondal, K., U.K. Chatterjee, and B.S. Murty, *Oxidation behavior of multicomponent Zr-based amorphous alloys.* Journal of Alloys and Compounds, 2007. **433**(1-2): p. 162-170.
79. Kai, W., Hsieh, H. H., Nieh, T. G., Kawamura, Y., *Oxidation behavior of a Zr-Al-Cl-Al-Ni amorphous alloy in air at 300-425 degree C.* Intermetallics, 2002. **10**: p. 1265-1270.

80. Kai, W., Hsieh, H. H., Chen, Y. R., Wang, Y. F., Dong, C., *Oxidation behavior of an Zr53Ni23.5Al23.5 bulk metallic glass at 400-600C.* Intermetallics, 2007. **15**(11): p. 1459-1465.
81. Vieregge, K. and C. Herzig, *Tracer diffusion of silver in alpha-zirconium single- and polycrystals.* Journal of Nuclear Materials, 1989. **165**(1): p. 65-73.
82. Kang, D.H. and I.-H. Jung, *Critical thermodynamic evaluation and optimization of the Ag-Zr, Cu-Zr and Ag-Cu-Zr systems and its applications to amorphous Cu-Zr-Ag alloys.* Intermetallics, 2010. **18**(5): p. 815-833.
83. He, X.C., Wang, H., Liu, H. S., Jin, Z. P., *Thermodynamic description of the Cu-Ag-Zr system.* Calphad, 2006. **30**(4): p. 367-374.
84. Chirkin, A.V., Gajum, Naima R., Ben Shaban, Asia I., Ramadan, Khaled Kher, *On the anisotropy of Zirconium and its alloys with Niobium.* Journal of Nuclear Materials, 1987. **148**(2): p. 171-174.
85. Asthana, R., M. Singh, and N. Sobczak, *Wetting behavior and interfacial microstructure of palladium- and silver-based braze alloys with C–C and SiC–SiC composites.* Journal of Materials Science, 2010. **45**(16): p. 4276-4290.
86. Fairchild, H.B., *The Properties of Zirconium and Its Possibilities for Thermal Reactors*, in *Power Pile Divison*1949, Oak Ridge Nation laboratory: Oak Ridge. p. 99.
87. Cao, Q.P., Li, J. F., Hu, Y., Horsewell, A., Jiang, J. Z., Zhou, Y. H., *Deformation-strengthening during rolling Cu60Zr20Ti20 bulk metallic glass.* Materials Science and Engineering: A, 2007. **457**(1-2): p. 94-99.
88. Zhang, C., Hui, X. Liu, X., Chen, G., *Preparation and Mechanical Properties of High Strength Zr-Based Bulk Metallic Glasses Containing High Content of Cu.* Rare Metal Materials and Engineering, 2008. **37**(2): p. 320-324.
89. Wang, W.H., C. Dong, and C.H. Shek, *Bulk metallic glasses.* Materials Science and Engineering: R: Reports, 2004. **44**(2-3): p. 45-89.
90. Zhang, W., Jia, F., Zhang, Q., Inoue, A., *Effects of additional Ag on the thermal stability and glass-forming ability of Cu-Zr binary glassy alloys.* Materials Science and Engineering: A, 2007. **459**(1-2): p. 330-336.
91. Xia, J.H., Qiang, J.B., Wang, Y.M., Wang, Q., Dong, C., *Cu-Zr-Ag bulk metallic glasses based on Cu8Zr5 icosahedron.* Materials Science and Engineering: A, 2007. **449-451**(0): p. 281-284.
92. Saida, J., Matsushita, M. Li, C. Inoue, A., *Effects of Ag and Pd on the nucleation and growth of the nano-icosahedral phase in Zr65Al7.5Ni10Cu7.5M10 (M = Ag or Pd) metallic glasses.* Philosophical Magazine Letters, 2000. **80**(11): p. 737-743.
93. A. Inoue, T.Z., M. W. Chen, T. Sakurai, J. Saida, and M. Matsushita, *Ductile quasicrystalline alloys.* Applied Physics Letters, 2000. **76**(8): p. 3.
94. M Matsushita, J.S., T Zhang, A Inoue, M W Chen, T Sakurai, *Grain growth behaviour of quasicrystals from the supercooled liquid region of Zr(65)Cu(7.5)Al(7.5)Ni(10)Ag(10) metallic glass.* Philosophical Magazine Letters, 2000. **80**(2): p. 79-84.
95. Chen, M.W., Zhang, T., Inoue, A., Sakai, A., and Sakurai, T. , *Quasicrystals in a partially devitrified ZrAlNiCuAg bulk metallic glass.* Applied Physics Letters, 1999. **75**: p. 1697.

96. Qin, W., Li, J. Kou, H., Gu, X., Xue, X., Zhou, L., *Effects of alloy addition on the improvement of glass forming ability and plasticity of Mg-Cu-Tb bulk metallic glass.* Intermetallics, 2009. **17**(4): p. 253-255.
97. Li, Z.G., Hui, X., Zhang, C.M., Chen, G.L., *Formation of Mg-Cu-Zn-Y bulk metallic glasses with compressive strength over gigapascal.* Journal of Alloys and Compounds, 2008. **454**: p. 168-173.
98. Zheng, Q., Cheng, S., Strader, J. H., Ma, E., Xu, J., *Critical size and strength of the best bulk metallic glass former in the Mg-Cu-Gd ternary system.* Scripta Materialia, 2007. **56**(2): p. 161-164.
99. Jiao, W., Zhao, K., Xi, X.K., Zhao, D.Q., Pan, M.X., Wang, W.H., *Zinc-based bulk metallic glasses.* Journal of Non-Crystalline Solids, 2010. **356**(35-36): p. 1867-1870.
100. Wang, G., Liaw, Peter K., Senkov, Oleg N., Miracle, Daniel B., Morrison, Mark L., *Mechanical and Fatigue Behavior of Ca65Mg15Zn20 Bulk-Metallic Glass.* Advanced Engineering Materials, 2009. **11**(1-2): p. 27-34.
101. Raphael, J., Wang, G., Liaw, P., Senkov, O., Miracle, D., *Fatigue and Fracture Behavior of a Ca-Based Bulk-Metallic Glass.* Metallurgical and Materials Transactions A, 2010. **41**(7): p. 1775-1779.
102. Senkov, O.N., D.B. Miracle, and J.M. Scott, *Development and characterization of Ca-Mg-Zn-Cu bulk metallic glasses.* Intermetallics, 2006. **14**(8-9): p. 1055-1060.
103. Akihisa, I., *Chapter 14 Bulk amorphous alloys*, in *Pergamon Materials Series*, C. Suryanarayana, Editor 1999, Pergamon. p. 375-415.
104. Liu, Y.H., Wang, K., Inoue, A., Sakurai, T., Chen, M.W., *Energetic criterion on the intrinsic ductility of bulk metallic glasses.* Scripta Materialia, 2010. **62**(8): p. 586-589.